Received: 7 October 2025 | Revised: 27 April 2026 | Accepted: 6 June 2026

DOI: 10.1002/qj.70248

Quarterly Journal of the Royal Meteorological Society RMetS

RESEARCH ARTICLE

Wavelet covariance approach to measure convective boundary-layer structure

Song-Lak Kang[1] | Cho-Rong Choi[1] | Jung-Hee Ryu[2]

[1]Department of Atmospheric and Environmental Sciences, Kangwon National University, Gangneung-si, Republic of Korea

[2]Institute for Smart Infrastructure, Kangwon National University, Gangneung-si, Republic of Korea

Correspondence
Jung-Hee Ryu, Institute for Smart Infrastructure, Kangwon National University, Gangneung-si, Republic of Korea.
Email: jhryu@kangwon.ac.kr

Funding information
National Research Foundation of Korea, Grant/Award Number: RS-2021-NR060132; Korea Meteorological Administration, Grant/Award Number: RS-2024-00404042; Gangwon RISE Center, Grant/Award Number: 2026-RISE-10-002

Abstract

The convective boundary layer (CBL) strongly influences moist convection and pollutant dispersion, yet objective diagnosis of its vertical structure from radiosondes remains challenging. Although Haar wavelet transforms have been employed to analyze CBL structure, most studies emphasize identifying a single boundary-layer top, typically inferred from a one-variable profile. We extend the application of the Haar discrete wavelet transform (DWT) to simultaneously analyze vertical profiles of potential temperature (θ) and water vapor mixing ratio (r). Rather than focusing solely on CBL height, the method decomposes profiles into multiscale means and deviations to diagnose multiple structural features, including surface-layer height, entrainment zone depth and intensity, and boundary-layer height. By leveraging wavelet localization and explicitly quantifying θ–r covariance across scales, the framework captures coupled thermodynamic transitions and reveals structural decoupling that may obscure layer boundaries in traditional gradient-based approaches. Applications to high-resolution radio sounding data from the International H_2O Project and the ARM Southern Great Plains Central Facility demonstrate that the method reliably captures canonical CBL structures, while objectively identifying atypical profiles characterized by diffuse gradients or θ–r decoupling. Sensitivity experiments on vertical resolution further reveal how coarse operational soundings smooth critical transitions and introduce systematic biases in diagnosed layer depths. Overall, this enhanced Haar wavelet framework advances CBL analysis from single-height detection toward comprehensive, scale-dependent structural diagnosis applicable to both research-grade and operational datasets.

KEYWORDS

convective boundary layer, entrainment zone, Haar discrete wavelet transform, multiscale, surface layer, vertical profiles

1 | INTRODUCTION

The Atmospheric Boundary Layer (ABL) is the lowest part of the troposphere directly influenced by the Earth's surface. Following sunrise, surface heating drives the growth of the ABL into a convective boundary layer (CBL) through buoyancy-driven thermals. The structure of the CBL plays a critical role in numerous atmospheric processes, including pollutant dispersion and the initiation of moist convection. Within the CBL, the surface layer (SL) and entrainment zone (EZ) are governed by fundamentally different processes, ranging from near-surface turbulent exchange to boundary-layer growth and the initiation of moist convection. Understanding the structure and properties of these layers is therefore essential for accurately representing CBL dynamics and its coupling to larger-scale atmospheric phenomena. Consequently, accurate estimation of the SL and EZ structures is essential for both environmental applications and meteorological studies (e.g., Kaimal & Finnigan, 1994; Stull, 1988).

Radio soundings provide routine vertical profiles of potential temperature (θ), water vapor mixing ratio (r), and wind, and they have long been used to diagnose boundary-layer structure. A variety of algorithms have been developed, including gradient methods based on θ or r (e.g., Li, Liu, *et al.*, 2021; Li, Zhang, *et al.*, 2021; Seidel *et al.*, 2010), parcel methods that track the lifting of near-surface air parcels (e.g., Holzworth, 1964; Seidel *et al.*, 2010), and bulk Richardson number criteria (e.g., Lee & Pal, 2021; Richardson, 1920; Richardson *et al.*, 2013; Vogelezang & Holtslag, 1996). While these approaches are useful, their performance depends strongly on stability regime, vertical resolution, and the presence of multilayer structures, often leading to substantial uncertainty in diagnosed boundary-layer depths. Integrated methods that combine thermodynamic variables with cloud indicators have also been explored (Wang *et al.*, 2014); however, challenges remain in consistently identifying EZ and SL heights from radiosonde profiles.

Beyond estimating a single boundary-layer height, resolving the detailed vertical structure of the CBL, particularly the SL and EZ, remains scientifically important yet observationally challenging. EZ is typically associated with enhanced thermodynamic gradients and variability near the CBL top, reflecting active entrainment processes that control boundary-layer growth and free-tropospheric coupling. In contrast, the SL is confined to the lowest several meters of the atmosphere, often within approximately 10 m of the surface, where standard radiosonde measurements provide limited vertical resolution and may be affected by sensor equilibration and launch-related adjustments. Consequently, although the CBL top can often be diagnosed with reasonable consistency, robust identification of SL height and quantitative characterization of EZ depth and intensity remain difficult using conventional radiosonde-based techniques.

Beyond traditional gradient-based criteria, recent studies have highlighted the sensitivity of diagnosed ABL heights to the detection methodology employed, particularly in complex tropical, coastal, and heterogeneous environments (Kakkanattu *et al.*, 2023a; Li, Liu, *et al.*, 2021; Li, Zhang, *et al.*, 2021; Mehta *et al.*, 2017). Intercomparison studies demonstrate that different algorithms applied to the same sounding can yield substantially different boundary-layer heights, especially under multilayered or weakly stratified conditions (Seidel *et al.*, 2010; Wang & Wang, 2014). In this context, automated techniques such as the wavelet covariance transform (WCT) have been increasingly adopted to improve objectivity and reproducibility (Baars *et al.*, 2008; Brooks, 2003; Davis *et al.*, 2000). In parallel, classification-based approaches, including fuzzy-logic framework, have been explored to account for ambiguous or diffuse structural transition (Kakkanattu *et al.*, 2023b). These studies collectively indicate that multilayer structures, residual layers, and gradual thermodynamic transitions can complicate boundary-layer identification, underscoring the importance of detection methods that are objective, robust to noise, and explicitly scale-aware.

The WCT has emerged as a particularly powerful tool for detecting step changes in vertical profiles. Unlike the maximum-gradient method, which identifies the boundary-layer top solely at the sharpest θ increase (Sullivan *et al.*, 1998), the WCT provides a scale-dependent framework that enhances localized transitions while preserving the structural information (e.g., Davis *et al.*, 2000). By operating across multiple scales, the WCT is less sensitive to noise and spurious fluctuations, making it more robust than single-gradient methods. Its objective formulation ensures reproducibility and makes it suitable for automated detection in large datasets.

Wavelet methods have been widely applied in remote sensing of the boundary layer. For example, Brooks (2003) used them with lidar backscatter for automated mixed-layer height detection, and Baars *et al.* (2008) demonstrated their utility for long-term ceilometer monitoring. Cohn and Angevine (2000) characterized mixed-layer and entrainment-zone thickness using lidar and wind profiler data, while Schmid and Niyogi (2012) introduced a radiosonde-based approach inspired by higher-order moments. Conventional radiosonde-based methods have also been systematically evaluated (Li, Liu, *et al.*, 2021; Li, Zhang, *et al.*, 2021), highlighting both their strength and limitations. Collectively, these studies demonstrate the promise of wavelet-based techniques, yet applications to radiosonde thermodynamic profiles remain limited. In particular, no framework has systematically exploited multiscale θ–r covariance to identify both SL and EZ structure. This gap motivates the development of a robust wavelet-based methodology tailored for radiosonde applications.

Building on this foundation, the present study introduces a Haar wavelet covariance approach to objectively characterize CBL structure from radiosonde measurements. The method exploits the localization property of a wavelet to detect sharp gradients in θ and r and to quantify their covariance, providing a consistent framework for identifying the SL, mixed layer (ML), and EZ. In particular, the EZ depth and intensity remain difficult to capture with conventional techniques. We evaluate the method using high-resolution radiosonde profiles from the International H_2O Project (IHOP_2002; Weckwerth *et al.*, 2004; LeMone *et al.*, 2007) and the Atmospheric Radiation Measurement (ARM) Southern Great Plains (SGP) Central Facility (Berg & Lamb, 2016) and further assess its sensitivity to vertical resolution to test applicability to operational soundings. The objectives of this paper are threefold: (1) to introduce the Haar wavelet covariance approach for radiosonde profiles, (2) to evaluate its performance in detecting the SL, ML, and EZ, and (3) to assess its applicability and limitations across a range of CBL conditions.

2 | WAVELET-BASED APPROACH

2.1 | Haar discrete wavelet transform

To extract the key parameters that characterize the CBL structure, we apply the Haar discrete wavelet transform (DWT) to vertical profiles of θ and r. The Haar DWT decomposes a vertical profile f (where f denotes either θ or r) into localized, scale-dependent components using an orthogonal set of wavelet basis functions. Because the Haar wavelet employs a step-function basis, it is particularly effective in detecting sharp transition in a signal (e.g., García-Franco *et al.*, 2021; Vickers & Mahrt, 2003). This property makes the Haar DWT well suited for quantifying CBL structure, as vertical profiles of θ and r typically exhibit sharp gradients at layer interfaces, such as the surface–mixed layer, mixed layer–entrainment zone, and entrainment zone–free atmosphere.

The Haar scaling function $\varphi_{j,k}(z_n)$ is defined in terms of the scale parameter j and the shift parameter k as

$$\varphi_{j,k}(z_n) = 2^{j/2}\,\varphi\left(2^j z_n - k\right), \tag{1}$$

where

$$\varphi\left(2^j z_n - k\right) = \begin{cases} 1, & \frac{k}{2^j} \le z_n < \frac{k+1}{2^j}, \\ 0 & \text{otherwise}. \end{cases} \tag{2}$$

Here, the normalized coordinate $z_n = n/N$ denotes the position of the input signal at index n within the unit interval [0, 1], where N is the total number of data points. Since $\varphi_{j,k}(z_n)$ represents the largest-scale trend of the profile, it is applied only at the coarsest scale ($j = 0$), where it spans the entire domain with a constant value of unity.

The Haar wavelet function $\psi_{j,k}(z_n)$ is similarly defined as

$$\psi_{j,k}(z_n) = 2^{j/2}\,\psi\left(2^j z_n - k\right), \tag{3}$$

where

$$\psi\left(2^j z_n - k\right) = \begin{cases} 1, & \frac{2k}{2^{j+1}} \le z_n < \frac{2k+1}{2^{j+1}}, \\ -1, & \frac{2k+1}{2^{j+1}} \le z_n < \frac{2(k+1)}{2^{j+1}}, \\ 0, & \text{otherwise}. \end{cases} \tag{4}$$

By scaling with the dyadic factor 2^j and translating by $k/2^j$, the wavelet function $\psi_{j,k}(z_n)$ represents localized fluctuations (detail components) of the signal at resolution level j.

Figure 1 illustrates the Haar scaling and wavelet functions across different scales j and shifts k. The scale parameter j determines the resolution of $\psi_{j,k}(z_n)$, with $j = 0, 1, \cdots, M-1$, where $N = 2^M$ represent the total number of data points in the profile. In this study, the radiosonde profiles were first interpolated onto a uniform vertical grid with about 5-m spacing from the surface to 5 km and then resampled to $N = 1024$ points ($M = 10$) to satisfy the dyadic-length requirement of the Haar DWT. At the coarsest scale ($j = 0$), the function spans the entire profile, capturing only the broadest trend. As j increases, the support of the function is halved at each step, providing progressively finer localization. For each scale j, the shift parameter k ranges from 0 to $2^j - 1$, specifying the position of the function within the domain.

The Haar DWT decomposes a vertical profile into one approximation coefficient, $W_\varphi(j,k)$, and a set of detail coefficients, $W_\psi(j,k)$, with 2^j segments at each scale j. The approximation coefficient $W_\varphi(j,k)$ represents the largest-scale trend of the profile and is computed only at the coarsest scale. In contrast, the detail coefficients $W_\psi(j,k)$ capture localized variations between adjacent subsegments and are computed recursively up to the chosen decomposition level M. This multiscale representation enables characterization of vertical variability as a function of height.

The original profile $f(z)$ can be reconstructed by applying the inverse Haar DWT, which progressively combines the approximation and detail coefficients:

$$f(z) = \frac{1}{\sqrt{N}}\left(W_\varphi(0,0)\varphi_{0,0}(z_n) + \sum_{j=0}^{j=M-1}\sum_{k=0}^{k=2^j-1} W_\psi(j,k)\psi_{j,k}(z_n) \right), \tag{5}$$

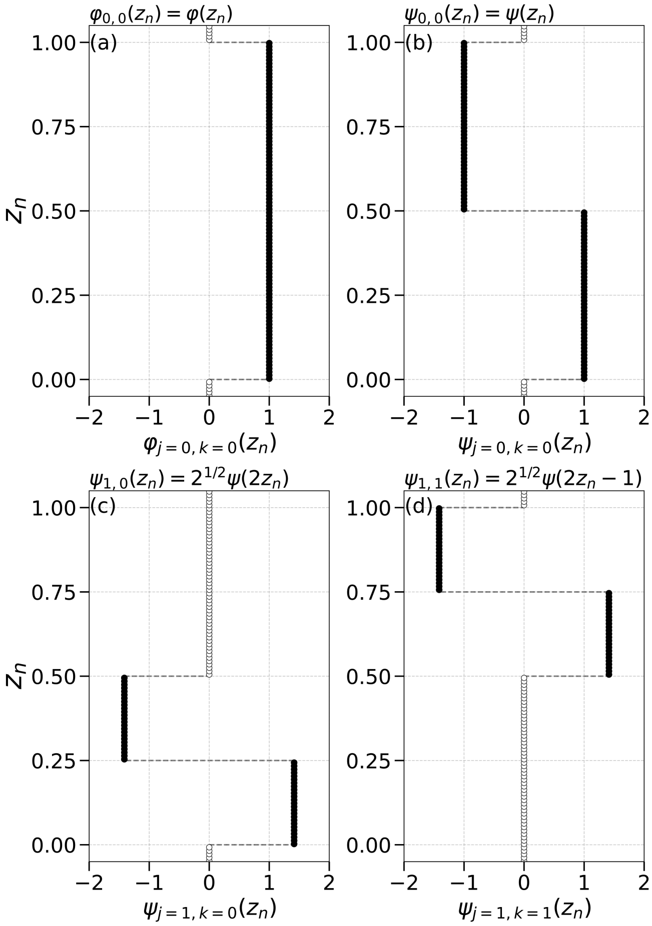

FIGURE 1 (a) Haar scaling function $\varphi_{j,k}(z_n)$ for $j = 0, k = 0$; and Haar wavelet functions $\psi_{j,k}(z_n)$ for (b) $j = 0, k = 0$, (c) $j = 1$, $k = 0$, (d) $j = 1, k = 1$

where N is the total number of data points. In this formulation, the first term represents the approximation component, denoted $cA_f^{(M)}$, and the second term represents the detail components, denoted $cD_f^{(m)}$, where $m = M - j$ specifies the scale. When $m = M$, the term corresponds to the entire data window, whereas smaller values of m represent progressively finer scales.

Figure 2a illustrates the decomposition of the vertical θ profile into the approximation coefficient $cA_\theta^{(M)}$ (with $M = 10$) and the set of detail coefficients $cD_\theta^{(m)}$ for $m = M,\ M-1,\ \cdots,\ 1$. The scaling function $\varphi_{0,0}(z_n)$ is constant across the domain and therefore mathematically equivalent to computing the arithmetic mean. Figure 2b shows the stepwise reconstruction of the vertical θ profile, in which $cA_\theta^{(M)}$ and $cD_\theta^{(m)}$ are progressively combined across scales. The rightmost panel of Figure 2b displays the fully reconstructed signal, demonstrating complete recovery of the original profile.

2.2 | Multiscale segment means and deviations

Using the Haar DWT, segment means can be consistently represented across multiple scales (Figure 2b). At the coarsest scale M (segment length 2^M), the profile reduces to a single constant mean, expressed as the approximation component:

$$\langle f \rangle = cA_f^{(M)}. \tag{6}$$

At a finer scale m (segment length 2^m), the segment mean is obtained recursively by adding the corresponding detail at scale m, which accounts for the increment from resolution $m+1$ to m:

$$\overline{f}^{(m)} = \overline{f}^{(m+1)} + cD_f^{(m)}. \tag{7}$$

The coarser-scale mean on the right-hand side can itself be expressed as the global mean plus the accumulated details from all scales finer than M down to $m+1$:

$$\overline{f}^{(m+1)} = \langle f \rangle + \sum_{j=m+1}^{M} cD_f^{(j)}. \tag{8}$$

In particular, at the coarsest scale $(m = M)$, the mean reduces to

$$\overline{f}^{(M)} = \langle f \rangle + cD_f^{(M)}. \tag{9}$$

At scale m, the localized deviation of the profile relative to the coarser mean is given by

$$f'^{(m)} = f - \overline{f}^{(m+1)} = \sum_{j=1}^{m} cD_f^{(j)}, \quad 1 \le m \le M-1. \tag{10}$$

Accordingly, the total perturbation relative to the global mean is recovered at the coarsest scale:

$$f'^{(M)} = f - \langle f \rangle = f - cA_f^{(M)} = \sum_{m=1}^{m=M} cD_f^{(m)}. \tag{11}$$

As the scale index j increases (and thus m decreases), the deviations $f'^{(m)}$ isolate progressively finer-scale structures. This multiresolution property of the Haar DWT is analogous to applying a sequence of high-pass filters with increasingly higher cutoff frequencies. At larger m, the deviations capture broad, coarser-scale fluctuations of the profile, while at smaller m, they emphasize fine-scale variability. In the limiting case of $m = 1$ $(j = M - 1)$, $f'^{(1)}$ retains only the finest-scale variations, whereas at $m = M$,

Quarterly Journal of the Royal Meteorological Society RMetS

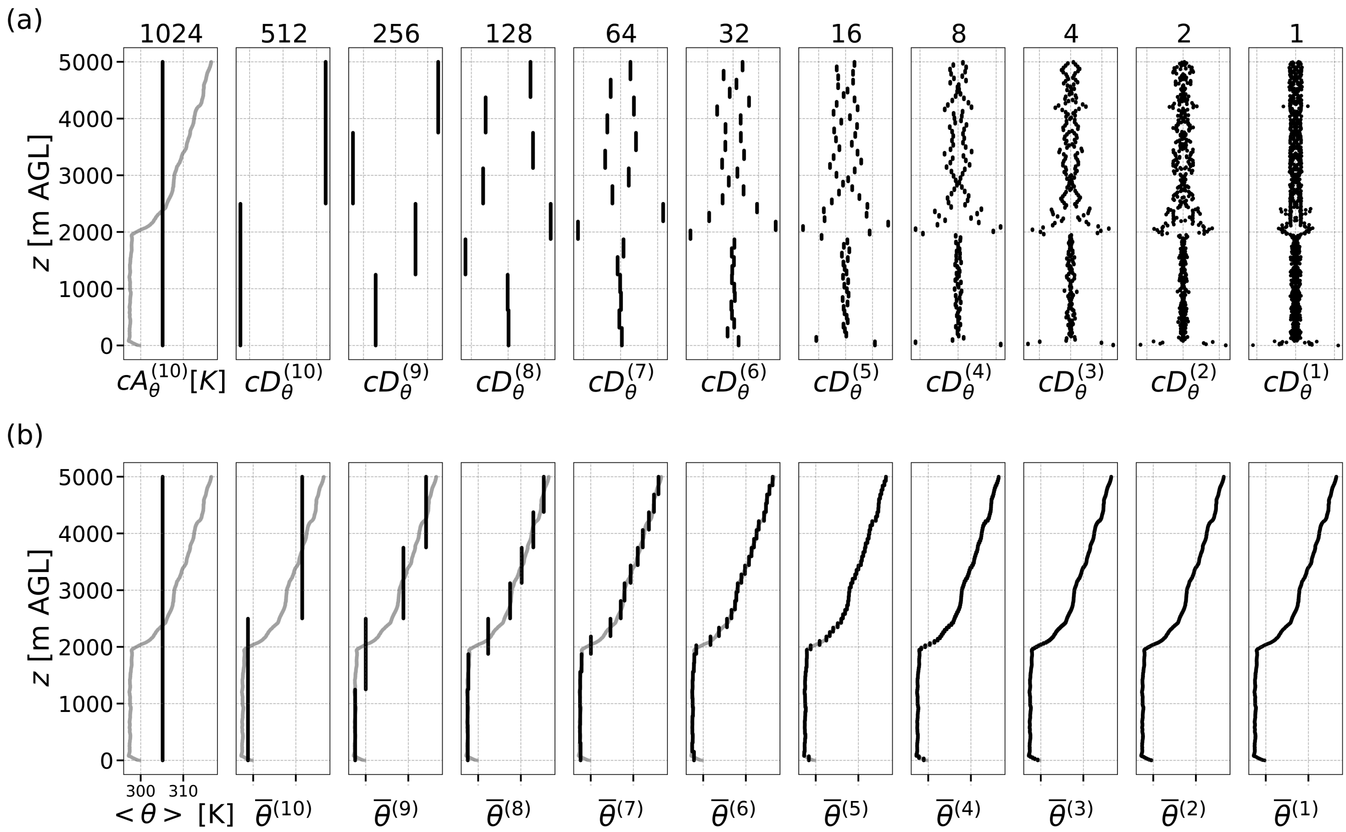

FIGURE 2 (a) Haar discrete wavelet transform (DWT, black lines) of the vertical profile of potential temperature (θ; gray line in the leftmost panel), consisting of 2^{10} (=1024) data points. The numbers above each panel indicate the number of data points per segment at each scale. At each scale, either the approximation coefficient $cA_\theta^{(10)}$ or the detail coefficients $cD_\theta^{(m)}$ ($m = 10, 9, \ldots, 1$) are shown. (b) Reconstruction of the profile obtained by progressively combining $cA_\theta^{(10)}$with the corresponding detail coefficients $cD_\theta^{(m)}$. AGL, above ground level

$f'^{(M)}$ represents the complete perturbation relative to the global mean.

2.3 | Multiscale θ–r covariances for CBL structure identification

Figure 3a conceptually illustrates vertical profiles of θ and r within the EZ of a typical CBL, along with their perturbations, θ' and r' defined relative to the corresponding segment means of $\overline{\theta}$ and $\overline{r}$. Within the EZ, θ increases with height while r decreases, i.e.,

$$\partial\theta/\partial z > 0, \partial r/\partial z < 0. \tag{12}$$

Above the level where the segment mean intersects each profile, θ' is predominantly positive while r' is predominantly negative, yielding $\theta' r' < 0$. Below this level, θ' becomes predominantly negative while r' becomes positive, so their product also remains negative. Consequently, $\overline{\theta' r'} < 0$ throughout the EZ segment. A covariance signal of the same sign may also occur in the free atmosphere (FA); however, its magnitude is typically much weaker. This weakening reflects two factors: the vertical gradients of θ and r are more gradual in the FA than across the EZ, and the relative absence of active turbulent mixing above the CBL prevents these background gradients from being converted into significant fluctuations. As a result, covariance magnitudes in the FA are generally negligible.

Figure 3b shows an analogous depiction of the SL, where θ and r both decrease with height, i.e.,

$$\partial\theta/\partial z < 0, \partial r/\partial z < 0 \tag{13}$$

In this case, above the level where the segment mean intersects each profile, θ' and r' are both predominantly negative, yielding $\overline{\theta' r'} > 0$. Below this level, θ' and r' become predominantly positive, and their product therefore also remains positive. Consequently, $\overline{\theta' r'} > 0$ throughout the SL segment. In the mixed layer, θ and r are generally well mixed and thus nearly uniform with height, so that $\overline{\theta' r'}$ remains close to zero.

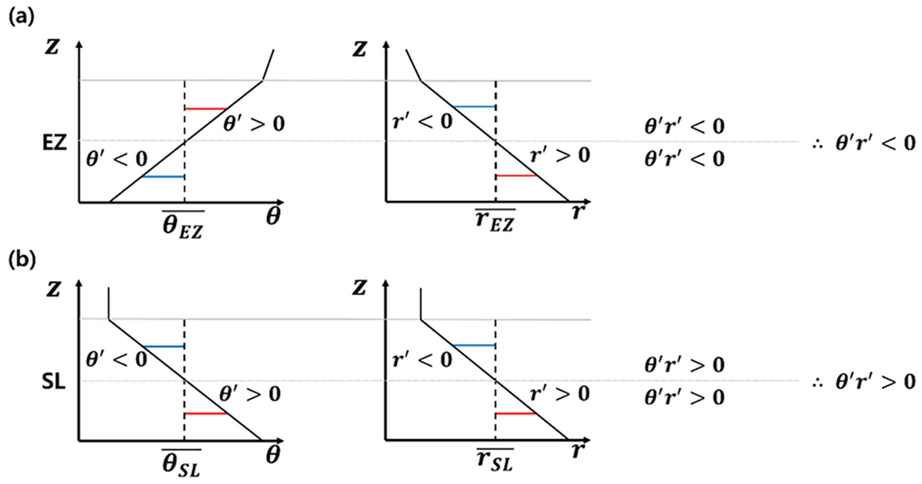

FIGURE 3 Perturbation products ($\theta' r'$) of potential temperature (θ) and water vapor mixing ratio (r) for (a) the entrainment zone (EZ) and (b) the surface layer (SL) of a canonical CBL. Solid black lines show the vertical profiles of θ and r, while dotted lines indicate their mean profiles $\overline{\theta}$ and $\overline{r}$. Perturbations θ' and r' are defined as deviations from these means, $\overline{\theta}$ and $\overline{r}$. Their products illustrate negative correlations in the EZ and positive correlations in the SL [Colour figure can be viewed at wileyonlinelibrary.com]

As defined in Equation (10), the Haar DWT-derived deviations of the vertical profiles, $\theta'^{(m)}(z)$ and $r'^{(m)}(z)$, are used to compute their product $\theta' r'^{(m)}(z)$ at each segment length of 2^m data points. Figure 4 shows example vertical profiles of $\theta'^{(m)}$, $r'^{(m)}$, and their product $\theta' r'^{(m)}$ in the vicinity of the EZ. From scale $m = M - 1 = 9$ downward, perturbation patterns consistent with the typical EZ structure (cf. Figure 3) emerge: $\theta'^{(m)} < 0$ below the level where the segment mean intersects the profile and $\theta'^{(m)} > 0$ above, whereas $r'^{(m)} > 0$ below and $r'^{(m)} < 0$ above, resulting in $\theta' r'^{(m)} < 0$ throughout the EZ. At the finest scale ($m = 1$), the product $\theta' r'^{(1)}$ remains negative across EZ, with its maximum absolute magnitude at the CBL top, thereby defining both the EZ and the CBL height.

2.4 | Algorithms for determining key CBL parameters

We now describe the algorithms used to determine four key parameters: the bottom of the EZ (h_0), the top of the EZ (h_2), the CBL height (z_i), and the top of the SL (z_{SL}). The identification of h_0, h_2, z_i, and z_{SL} is based on the covariance structure between θ and r derived from the Haar DWT analysis of the vertical profiles.

During method development, we verified that the covariance structure was broadly consistent with the expected slope conditions of θ and r described in Equations (12) and (13). These slope conditions are presented only to illustrate the conceptual relationship between the vertical structures of θ and r and the sign of their covariance within the EZ and SL.

The identification of the EZ bottom, h_0, proceeds in a two-step sequence to ensure physical robustness. First, an initial candidate level is defined as the lowest level at the finest scale ($m = 1$) for which the scale-1 covariance between θ and r becomes negative:

$$C(z) \equiv \theta' r'^{(1)}(z) < 0 \tag{14}$$

where $C(z)$ denotes the scale-1 covariance profile obtained from the Haar-DWT analysis (example shown in Figure 4). This primary condition identifies the potential onset of the anti-correlated thermodynamic-moisture structure characteristic of the entrainment zone.

To ensure that the detected covariance signal corresponds to a physically consistent EZ structure, the first-guess grid points are filtered using the signs of the vertical gradients of θ and r. Specifically, grid points are excluded if they satisfy $\partial\theta/\partial z \le 0$, $\partial r/\partial z \ge 0$, or both, as such combinations are inconsistent with the canonical EZ structure. These gradients are computed using a forward-difference method and are used only as a physical consistency filter rather than as a primary detection criterion. To ensure a reliable evaluation of these gradients, the vertical grid spacing must be finer than approximately 30 m.

Beyond these physical consistency checks, the candidate level h_0 is subjected to a final quantitative validation test to avoid misidentifying sporadic or transient negative covariance signals within the mixed layer as the EZ bottom. Specifically, the magnitude of the covariance at the candidate level is compared with the mean covariance magnitude within a prescribed window immediately above:

$$\left|C\left(h_{0,fg}\right)\right| > \alpha \frac{1}{n} \sum_{z_{\min}}^{z_{\max}} |C(z)|, \tag{15}$$

where n is the number of vertical levels within the averaging interval $z_{\min} = h_{0,fg}$, and $z_{\max} = h_{0,fg} + \Delta z_{h_0,fg}$. The coefficient α is an empirically determined threshold set to 0.8. This value was selected based on sensitivity tests conducted during algorithm development, which indicated

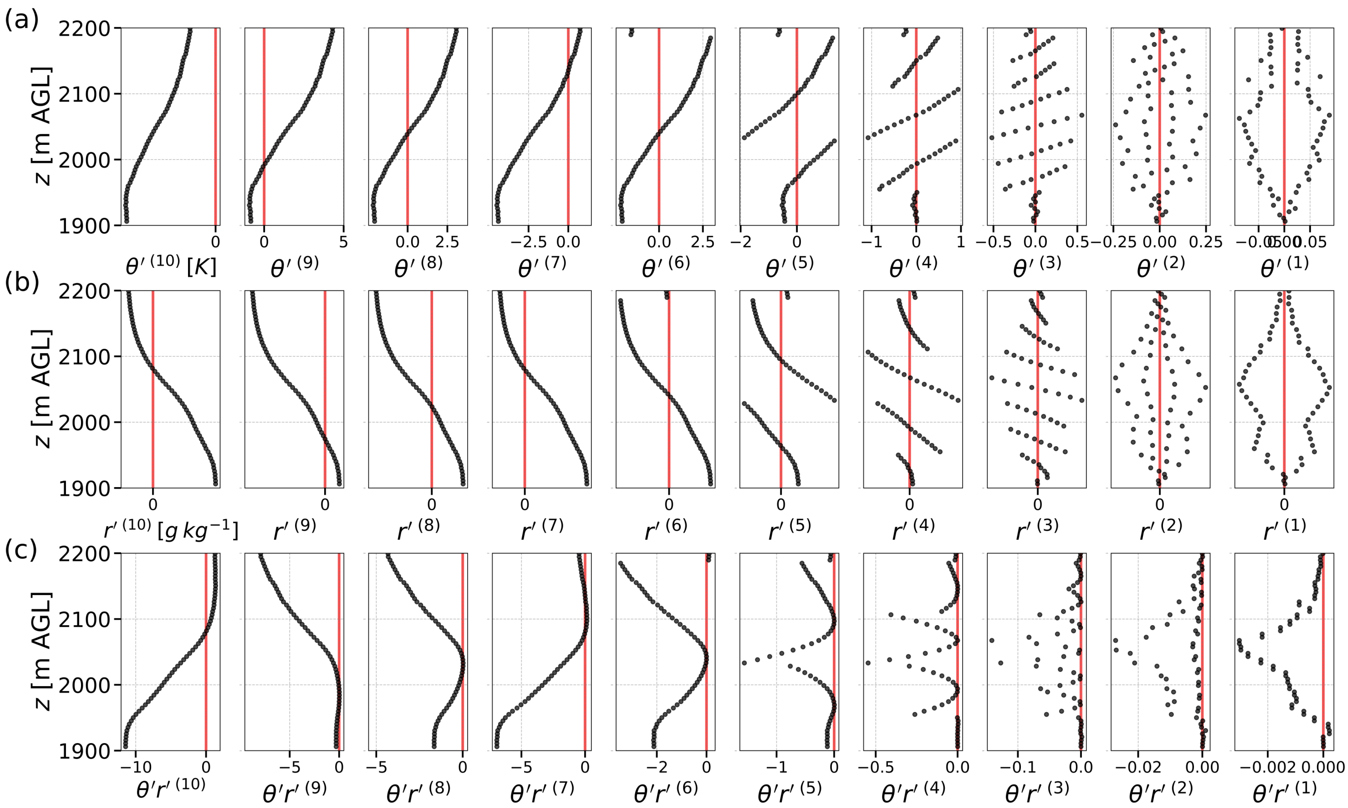

FIGURE 4 Vertical profiles of (a) potential temperature perturbation $\theta'^{(m)}$, (b) water vapor mixing ratio perturbation $r'^{(m)}$, and (c) their product $\theta' r'^{(m)}$ across scales within the entrainment zone (EZ). The red vertical line denotes zero. The leftmost panel shows the total perturbation, while subsequent panels illustrate scale-dependent deviations. The scale index decreases from left to right, representing progressively finer segment length. AGL, above ground level [Colour figure can be viewed at wileyonlinelibrary.com]

that $\alpha = 0.8$ provides an optimal balance: it effectively suppresses sporadic covariance noise in the mixed layer while retaining the robust, sustained covariance signature that defines the base of EZ.

The depth of the averaging window is defined as

$$\Delta Z_{h_0,fg} = \min\left(z_{\mathrm{Top}} - h_{0,fg}, 2\ \mathrm{km}\right), \tag{16}$$

which constrains the averaging interval above the candidate level. The upper limit of 2 km was introduced based on empirical examination of the sounding datasets used in this study, which showed that sporadic ML covariance signals rarely occur more than about 2 km above the entrainment zone. This constraint prevents the averaging interval from extending too deeply into the free troposphere while still allowing a sufficient vertical range to characterize the background covariance magnitude. At the same time, the window depth is also limited by the remaining distance to the upper search boundary z_{Top} (set to 5 km in this study), ensuring that the averaging interval does not exceed the available profile depth above the candidate level.

The summation in Equation (15) represents the arithmetic mean of $|C(z)|$ over the specified vertical interval. The final estimate of h_0 is defined as the lowest level within the range $300\ \mathrm{m} \le z \le z_{\mathrm{Top}}$, ($z_{\mathrm{Top}} = 5$ km) that satisfies both Equations (14) and (15). The lower bound of 300 m was introduced to avoid detecting sporadic covariance signals in the immediate near-surface layer, where strong gradients and measurement noise may occur. At the same time, this threshold remains sufficiently low to capture the entrainment zone base under typical CBL conditions.

Figure 5 illustrates the application of Equations (14) and (15) for estimating h_0, using a rawinsonde sounding from the ARM SGP Central Facility (CF; 36.605 °N, 97.485°W) near Lamont, Oklahoma, United States, at 11:30 LST (LST = UTC − 6) on 21 May 2009. The filtering step of E CBL quation (15) retains only those candidates where the negative covariance signal is significantly stronger than the surrounding background variability, thereby suppressing spurious detections from isolated negative covariance points within the mixed layer. This enhances the robustness of the wavelet-based identification of the EZ lower boundary. To demonstrate that this filtering is robust across varying boundary-layer structure, Figure 6 presents additional examples. These cases,

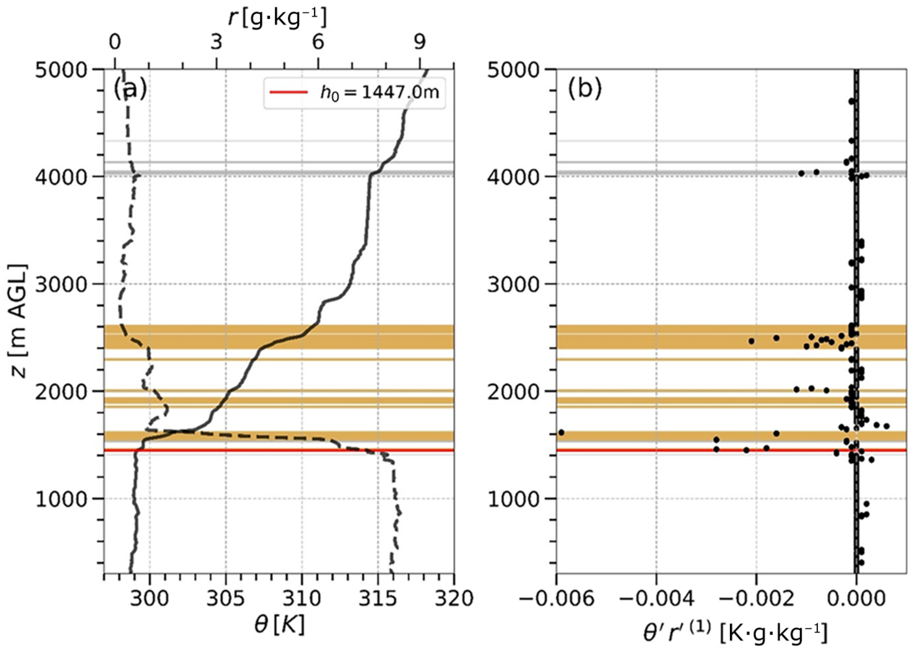

FIGURE 5 (a) Vertical profile of potential temperature (θ, solid) and water vapor mixing ratio (r, dashed), and (b) the scale-1 covariance ($\theta' r'^{(1)}$), observed at 11:30 LST on 21 May 2009 at the ARM SGP Central Facility (36.605°N, 97.458°W). Orange lines indicate candidate h_0 levels satisfying both Equations (14) and (15), while a gray line mark candidates satisfying Equation (14) only. The red line denotes the final h_0 at 1447 m. Panel (b) is plotted over a narrower X-axis range near zero to highlight the covariance structure around h_0. The minimum value of the full covariance profile is −0.033. AGL, above ground level [Colour figure can be viewed at wileyonlinelibrary.com]

from the ARM SGP CF (31 August 2009) and the IHOP 2002 Homestead (20 and 21 June 2002), confirm that the algorithm consistently isolates the sustained EZ signature from transient mixed-layer noise, even under different stability and moisture profiles. This cross-case validation underscores the reliability of the wavelet-based identification of the EZ boundaries.

The top of the EZ, h_2, is defined as the highest level within the interval $[h_0, h_0 + \Delta EZ_{fg}]$ that satisfies the condition given in Equations (14) and (15), such that:

$$h_2 = \max\left(z \in \left[h_0, h_0 + \Delta \mathrm{EZ}_{fg}\right] \mid \mathrm{Eq.14} \wedge \mathrm{Eq.\ 15}\right). \quad (17)$$

The thickness of the search interval is specified as

$$\Delta EZ_{fg} = \min\left(z_{\mathrm{Top}} - h_0, \beta_{\mathrm{EZ}} h_0\right), \quad (18)$$

where $\beta_{\mathrm{EZ}} = 0.5$. This parameter limits the maximum depth of the entrainment-zone search region to either the remaining profile extent above h_0 or a fraction of the mixed-layer depth proportional to h_0. The value $\beta_{\mathrm{EZ}} = 0.5$ was selected based on commonly reported entrainment-zone thicknesses in convective boundary layers, which typically scale with the intensity of thermals and represent a fraction of the mixed-layer depth. This scaling is broadly consistent with the empirical relation $h_0 \approx 0.8z_i$ reported in previous boundary-layer studies (e.g., Kaimal and Finnigan, 1997; Stull,1988). Sensitivity tests using alternative values between 0.3 and 0.7 showed that the estimated h_2 varied only slightly, indicating that the algorithm is relatively insensitive to the precise choice of β_{EZ}.

Figure 7 illustrates the application of Equations (14) and (15) for estimating h_2, using the same sounding shown in Figure 5. In this example, h_0 is 1447 m (see Figure 5). The first-guess depth, $\Delta \mathrm{EZ}_{fg}$, is determined from Equation (18) as 723 m, corresponding to the minimum of $z_{\mathrm{Top}} - h_0 = 3.553$ km and $\beta_{\mathrm{EZ}} h_0 = 723$ m. Within this interval candidate levels of h_2 are sequentially tested against Equations (14) and (15). The highest level that satisfies all the conditions is then selected as the final h_2, which is 1637 m in for this sounding.

Although Equation (15) is not among the theoretical conditions introduced in Section 2.3 for determining h_2, it is applied in practice to reduce the overestimation that often arises when Equation (14) is used alone. By emphasizing regions with strong negative covariance signals, Equation (15) improves the robustness of EZ top detection. Physically, h_2 corresponds to the level reached by overshooting updraft plumes above the mixed-layer top. The CBL height, z_i, is then defined as the midpoint between the EZ bottom (h_0) and the top (h_2), while the EZ thickness, ΔEZ, is given by their difference ($h_2 - h_0$).

At the base of the vertical profiles of θ and r, the SL condition given in Equation (13) is first evaluated within a shallow near-surface layer (here, between 10 and 35 m) to identify and exclude cases that do not satisfy the SL condition. Specifically, the SL top is defined as the lowest level above which a distinct ML emerges, characterized by nearly constant vertical gradients of θ and r.

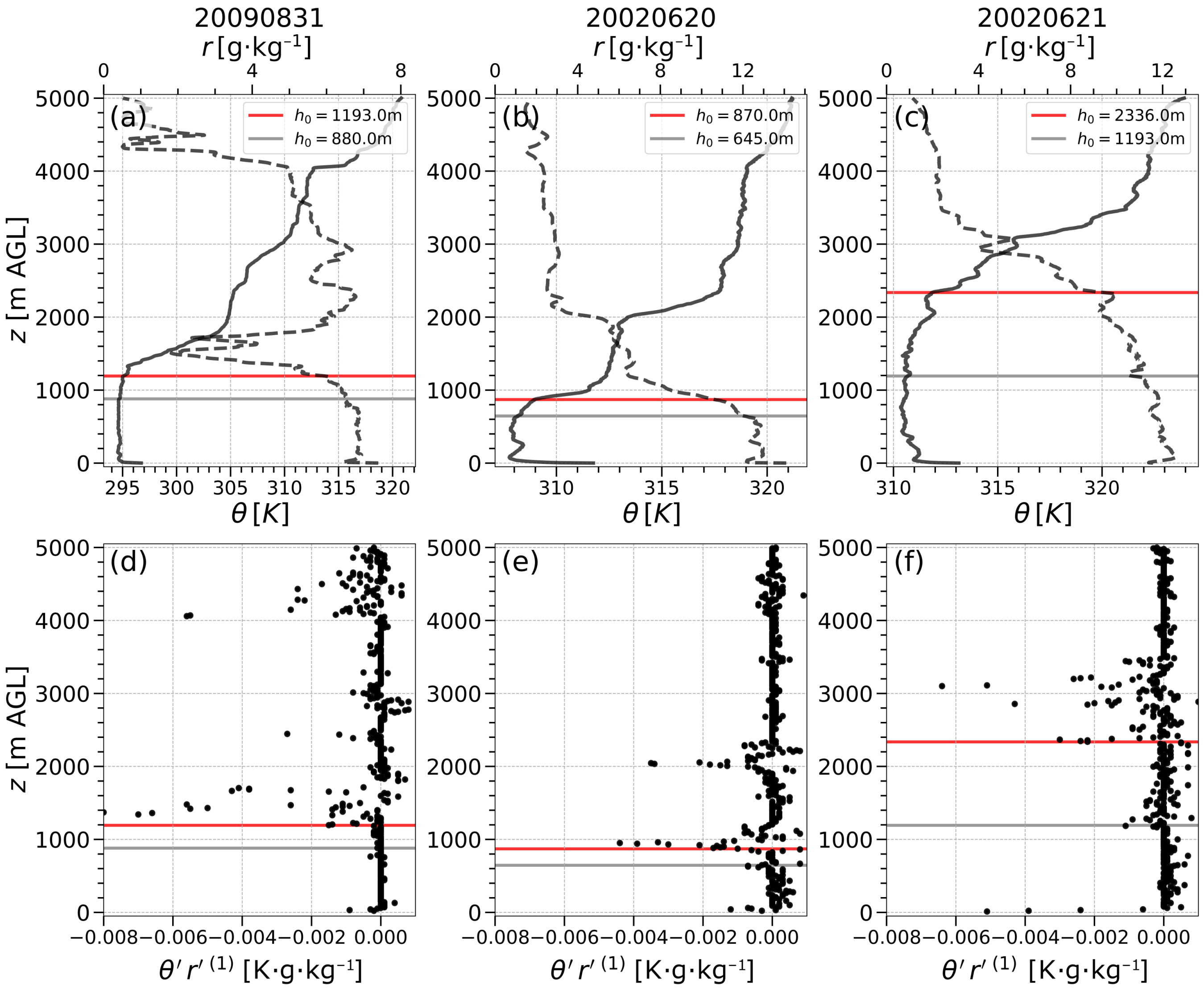

FIGURE 6 Three examples of vertical profiles exhibiting not-well-mixed structures within the mixed layer. In each case, the entrainment-zone bottom (h_0) is first identified using Equation (14) alone (horizontal gray line) and then corrected when both Equations (14) and (15) are applied (horizontal red line). The upper panels (a–c) show θ and r soundings, while the lower panels (d–f) present the corresponding scale-1 covariance ($\theta' r'^{(1)}$). Panels (a,d) display a sounding observed at ARM SGP Central Facility at 11:30 LST on 31 August 2009. Panel (b,e) and (c,f) show soundings from the IHOP_2002 campaign at 12:02 LST on 20 June 2002 and 13:39 LST on 21 June 2002, respectively. AGL, above ground level [Colour figure can be viewed at wileyonlinelibrary.com]

Accordingly, the SL top z_{SL} is determined as the level immediately below where the Haar-DWT scale-1 covariance of θ and r becomes zero:

$$\theta' r'^{(1)}(z > z_{\mathrm{SL}}) = 0. \tag{19}$$

An additional requirement is imposed to ensure physical consistency, namely that the covariance ($\theta' r'^{(1)}$) remains positive at levels below z_{SL}, consistent with the theoretical vertical structure of θ' and r' within the SL:

$$\theta' r'^{(1)}(z \le z_{\mathrm{SL}}) > 0. \tag{20}$$

Thus, the SL top is defined as the lowest level within the range $[z_2, \beta_{\mathrm{SL}} h_0]$ that simultaneously satisfies Equations (19) and (20):

$$z_{\mathrm{SL}} = \min\left(z \in \left[z_2, \beta_{SL} h_0\right] \middle| \text{Eq. 19} \wedge \text{Eq. 20}\right) \tag{21}$$

Here, z_2 denotes the second vertical data point, chosen to reduce potential noise contamination near the surface. The parameter β_{SL} defines the upper bound of the SL search interval and is set to $\beta_{\mathrm{SL}} = 0.5$. This bound ensures that the entire SL is included in the search while preventing contamination from the overlying ML. Although the

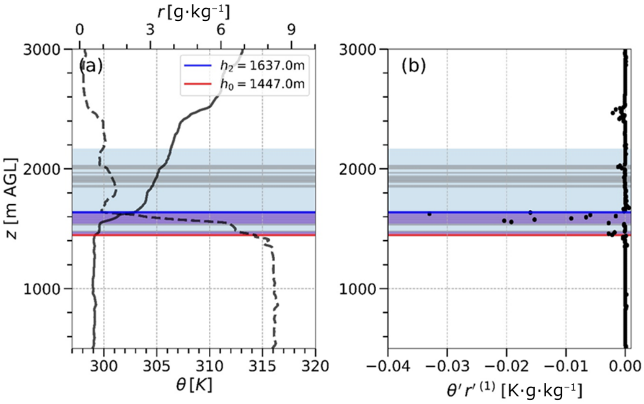

FIGURE 7 Same as Figure 5, but for the height range 500–3000 m. The estimated entrainment-zone (EZ) bottom (h_0 = 1447 m) is marked in red. The shaded region indicates the first-guess depth ΔEZ_{fg} defined by Equation (18), which is 723 m for this profile and serves as the search interval for h_2. Candidate levels of h_2 that satisfy both Equations (14) and (15) are shown in purple, while those satisfying Equation (14) only are shown in gray. The final h_2, determined as 1637 m, is marked by the blue line. AGL, above ground level [Colour figure can be viewed at wileyonlinelibrary.com]

SL typically occupies the lowest approximately 10% of the boundary-layer depth (Stull, 1988), a larger upper bound is adopted to ensure robustness under varying vertical sampling resolutions. Sensitivity experiments indicated that using β_{SL} values between 0.3 and 0.6 produces nearly identical z_{SL} estimates for most cases.

In practice, some individual points within the SL may not strictly satisfy Equation (20) because of the inherently turbulent nature of the SL. Therefore, when Equation (20) is not fulfilled at all levels, the mean covariance across the SL is instead required to remain positive:

$$\frac{1}{n}\sum_{z_2}^{z_{SL}} C(z) > 0 \tag{22}$$

Figure 8 illustrates the application of these conditions (Equations 19–21) together with the search interval [z_2, $\beta_{SL} h_0$], resulting in an identified z_{SL} of 98 m for this example.

3 | APPLICATIONS TO OBSERVATIONAL SOUNDINGS

3.1 | High-resolution radio soundings

We applied the wavelet approach to high-resolution radio soundings from two field datasets. The first dataset was collected with the Integrated Sounding System (ISS) deployed during the International H_2O Project (IHOP_2002; Weckwerth *et al.*, 2004; LeMone *et al.*, 2007), conducted over the Southern Great Plains from 13 May to 25 June 2002. The ISS provided frequent radiosonde launches with detailed profiles of temperature, humidity, and winds, which have been widely used to evaluate large-eddy simulations (LESs) of CBLs (e.g., Conzemius & Fedorovich, 2008; Couvreux *et al.*, 2005) and to document their observed evolution (Bennett *et al.*, 2010). From a total of 137 soundings, we initially selected 84 daytime launches between 10:00 and 17:00 LST. To ensure consistency with the 5-km analysis depth, we excluded three profiles with maximum vertical spacing exceeding 1 km and two profiles terminating near 4 km and 200 m respectively, leaving 79 soundings for analysis.

The second dataset consists of routine balloon-borne radio soundings from the US Department of Energy ARM Southern Great Plains (SGP) Central Facility near Lamont, Oklahoma (36.6° N, 97.5° W; 315 m mean sea level). These soundings, archived as the sgpsondewnpnC1 product (https://adc.arm.gov/), have been conducted four times daily (0530, 1130, 1730, and 2330 UTC) since 2001, with a nominal vertical resolution of 2 s. For this study, we analyzed profiles collected between May and September 2009, focusing on launches at 1730 UTC (11:30 LST). Of 153 scheduled launches, 149 were successfully completed; three were missing, and one was excluded because the ascent terminated near 2 km. Three supplemental launches (13:54 LST on 13 May, 14:46 LST on 9 June, and 10:02 LST on 2 August) were included, resulting in a total of 152 soundings retained for analysis.

Because the vertical resolution varies among individual sounding profiles, all profiles were interpolated onto a uniform vertical grid with a spacing of 5 m from the surface to 5 km. This spacing lies within the observational vertical-resolution ranges of both the IHOP (2.4–6 m) and ARM SGP (4.3–11.7 m) soundings at the lowest 5 km. The interpolated profiles were then resampled to 1024 data points (2^{10}) to satisfy the dyadic-length requirement of the Haar DWT, following Vickers and Mahrt (2003). The 231 soundings analyzed (79 from IHOP_2002 and 152 from ARM SGP) were classified into canonical, atypical, and unclassified CBL cases (Table 1). Here, In the canonical cases, the algorithm retrieved CBL parameters in close agreement with visual inspection, providing a robust baseline for typical CBL structures. Canonical examples are shown in Figure 9, where the algorithm accurately identified h_0 at the top of the ML, h_2 near the upper boundary of the EZ where the vertical gradients of θ and r change, and z_{SL} just below the ML base, delineating the SL where both θ and r decrease with height.

In contrast, parameter estimation for atypical cases was more challenging, although some profiles still yielded reasonable agreement. Three categories of atypical CBL

Quarterly Journal of the Royal Meteorological Society RMetS

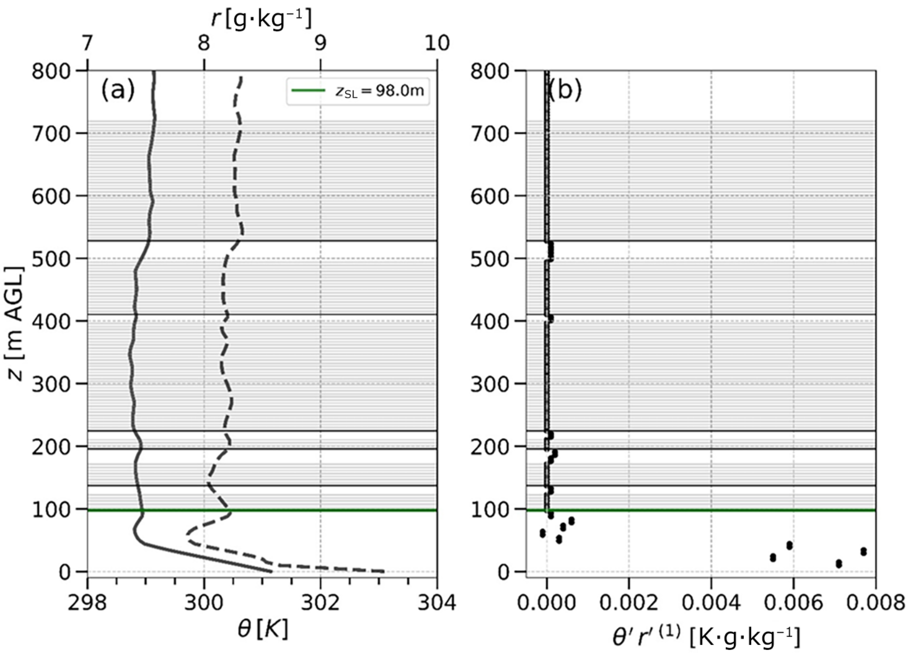

FIGURE 8 Same as Figure 5 but for the height range 0–800 m. Black lines mark levels that satisfy both Equations (19) and (20), whereas gray lines denote levels satisfying Equation (19) alone. The search for z_{SL} is performed over the interval $[z_2, \beta_{SL} h_0] = [10\ \text{m}, 0.5 \times 1447\ \text{m}]$. Following Equation (21), which selects the lowest level within this interval that meets both conditions, the final z_{SL} is identified at 98 m (horizontal green line). AGL, above ground level [Colour figure can be viewed at wileyonlinelibrary.com]

TABLE 1 Summary of 231 soundings from the IHOP_2002 and ARM datasets, classified into canonical, atypical, and unclassified categories. CBL, convective boundary layer

Case	Counts	Total (%)
Canonical CBL	110	47.6
Atypical: Not-well-mixed	57	24.7
Atypical: Ambiguous h_2	13	5.6
Atypical: $\theta - r$ decoupled	24	10.4
Unclassified	27	11.7
Total	231	100.0

structures were identified: not well mixed, ambiguous h_2, and θ–r decoupled. In not-well-mixed cases, large fluctuations within the ML obscure the covariance signal, causing the algorithm to misinterpret h_0 as an internal level within the ML, in turn leading to misidentification of the h_2 and an erroneous estimate of z_i. This limitation suggests that strong variability within the ML can hinder reliable detection of h_0. Nevertheless, when the covariance signal near the EZ remains sufficiently strong despite such fluctuations, the algorithm can still yield stable estimates (Figure 10a–c).

In ambiguous-h_2 cases, illustrated in Figure 10d–f, the vertical gradients of θ and/or r across the EZ are nearly uniform, resulting in a weak and diffuse covariance signature. Under these conditions, the covariance within the first-guess EZ depth (ΔEZ_{fg}) often lacks a distinct peak that clearly delineates the EZ top. Consequently, the algorithm tends to assign h_2 to the uppermost level within ΔEZ_{fg} based on the default threshold ($\beta_{\text{EZ}} = 0.5$). A representative example is shown in Figure 10f, where the identified EZ depth appears relatively shallow. However, sensitivity tests (not shown) indicate that by increasing the threshold β_{EZ} to 1.0, the algorithm can capture a much higher EZ top at approximately 800 m. This suggests that in certain cases, such as developing morning CBLs where the EZ depth can be as large as the ML depth (e.g., Stouffer *et al.*, 2025), the default search range may lead to an underestimation. For the purpose of this study, however, the default value was maintained to ensure robust performance across the broader midday-centered dataset.

The $\theta - r$ decoupled cases present a distinct challenge. In these profiles, θ exhibits a marked gradient change at a lower level, while r retains ML characteristics and shifts its gradient to a higher altitude. This mismatch weakens the covariance signal and often causes the algorithm to assign h_0 to the level where r shows a slope change, since both variables are evaluated simultaneously. In the 23 May 2002 sounding (Figure 10g), h_0 is identified at the height where the gradient in r is well defined. In another example, on the 15 September 2009 sounding (Figure 10i), θ develops a positive gradient while r remains nearly constant within the ML, resulting in h_0 being placed at the level where r eventually exhibits a negative gradient aloft. These vertical offsets appear to reflect divergent environmental forcings. On 15 September 2009, for example, antecedent rainfall coupled with northerly winds likely sustained high moisture levels above the thermal ML. The northerly flow continued

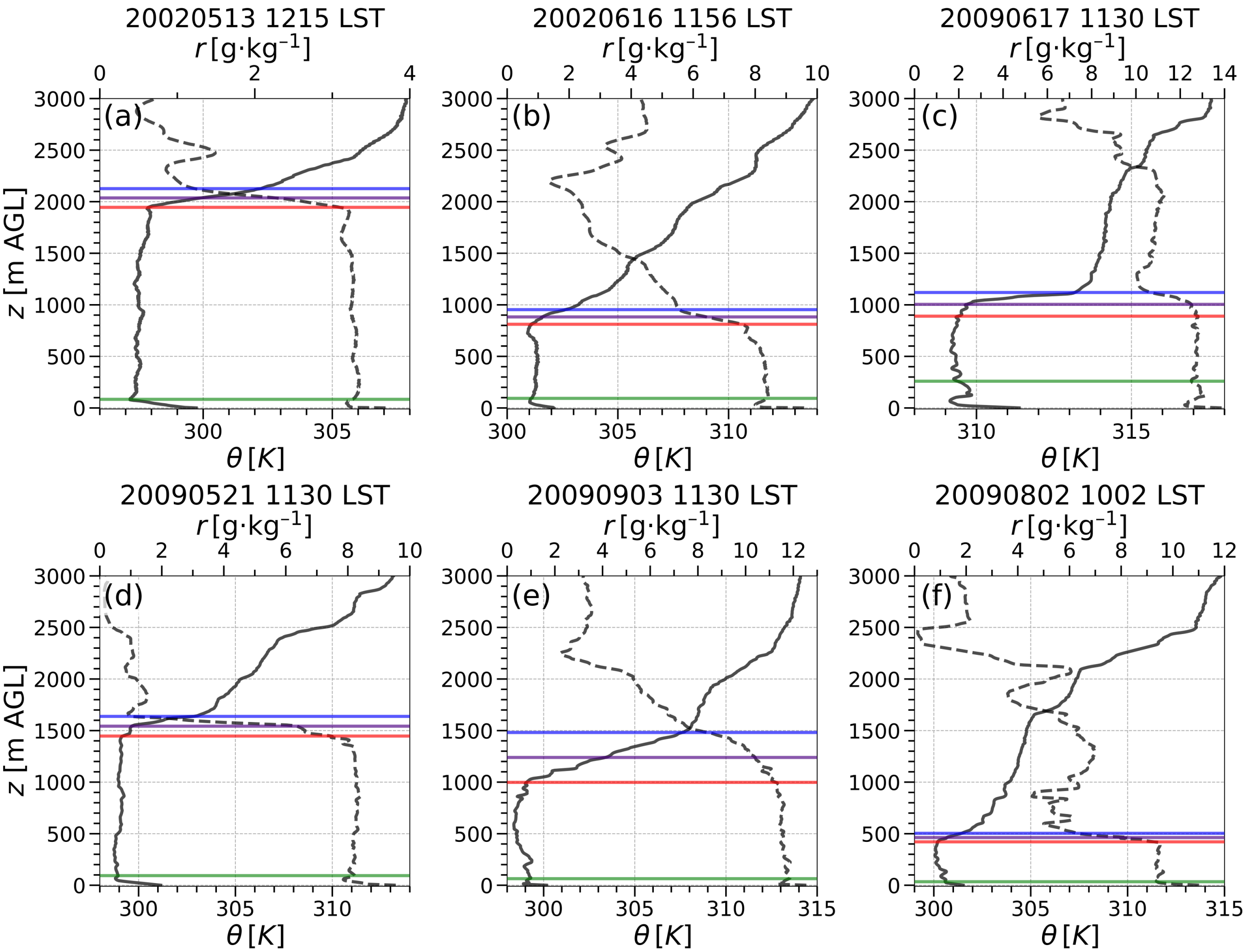

FIGURE 9 Six example profiles of potential temperature (θ, solid) and water vapor mixing ratio (r, dashed) selected from (a,b) IHOP_2002, and (c–f) ARM SGP datasets, illustrating canonical convective boundary layer (CBL) structures. Horizontal lines indicate key CBL parameters: The entrainment-zone (EZ) bottom (h_0, red), EZ top (h_2, blue), boundary-layer height (zi, purple), and surface-layer top (z_{SL}, green). AGL, above ground level [Colour figure can be viewed at wileyonlinelibrary.com]

to advect moisture into the region after passing over the nearby river, effectively "decoupling" the moisture profile from the thermal structure.

Twenty seven cases (11.7%; Table 1) could not be classified as either canonical or atypical and were grouped as unclassified, as the θ and r profiles lacked characteristic ML or EZ structures and exhibited irregular covariance signals. Overall, the algorithm captured CBL parameters reliably in canonical cases and showed mixed performance in atypical cases, yielding stable estimates in some profiles but inconsistent results for others.

The statistics of key CBL parameters derived from 110 canonical soundings in the high-resolution radiosonde datasets are summarized in Table 2. The mean and median CBL heights (1168 and 1066 m above ground level [AGL], respectively) indicate a characteristic depth of approximately 1 km. Similarly, the mean and median SL heights, derived from 85 soundings with a well-defined SL, are 89 and 83 m AGL, respectively. These values are slightly below the nominal 100 m depth, corresponding to roughly 10% of the CBL depth. Because the soundings were selected solely based on profile shape, without regard to weather regime, representative values of CBL height and SL depth can be taken as about 1 km and 80 m AGL, respectively, consistent with the expected ranges for well-developed daytime boundary layers (e.g., Sullivan *et al.*, 1998; Sullivan & Patton, 2011). The mean and median EZ thicknesses ($\Delta EZ = h_2 - h_0$) are 257 and 210 m, respectively, which fall within the 50–300 m range reported in LESs and field observations of CBLs (e.g., Huang *et al.*, 2011; Sullivan *et al.*, 1998). The corresponding mean and median vertical gradient of θ across the EZ are 1.9 and 1.3 K·(100 m)$^{-1}$, while those of r are 2.4 and 1.5 g·kg^{-1}·(100 m)$^{-1}$. These magnitudes are

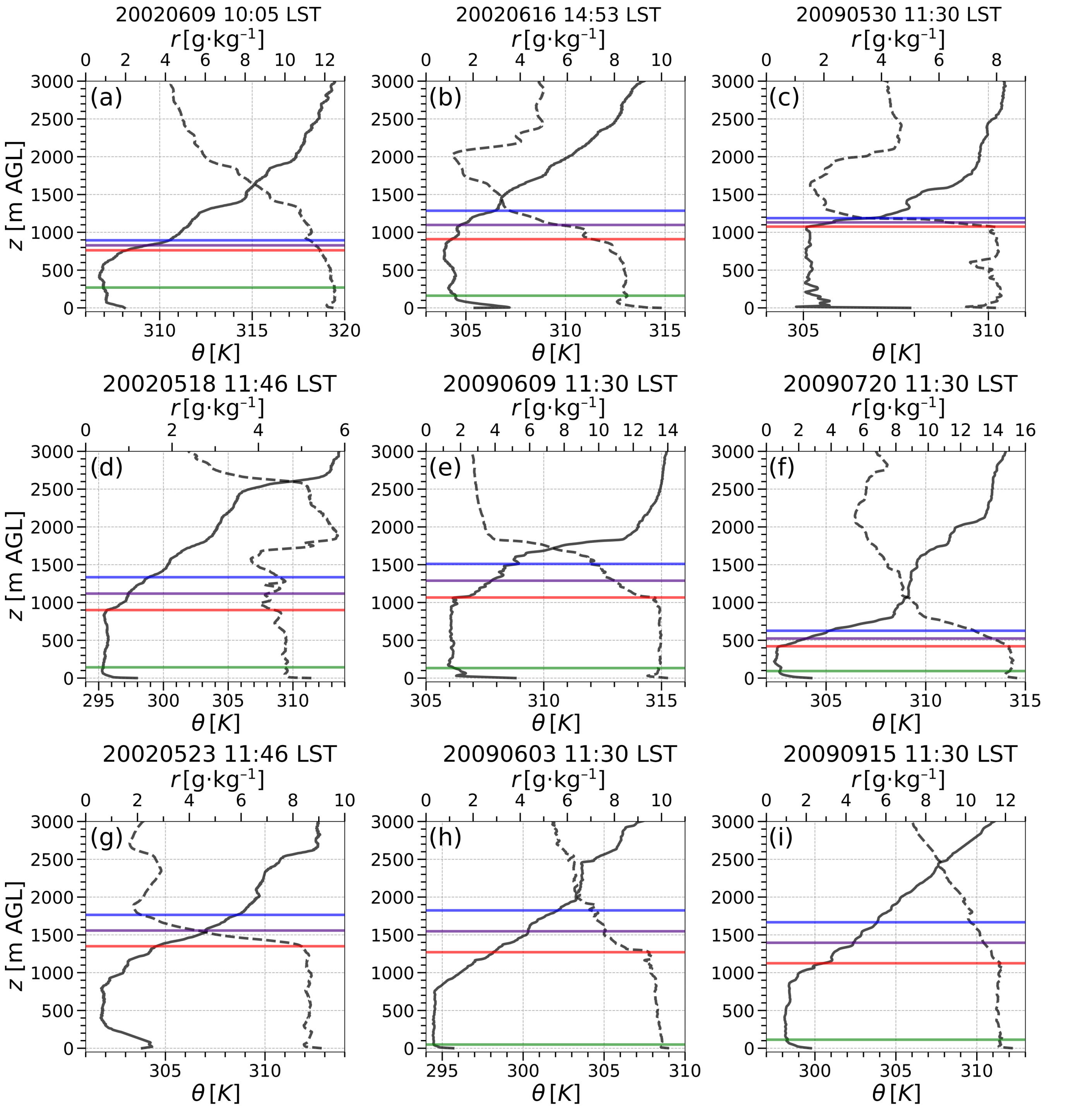

FIGURE 10 Nine example profiles of potential temperature (θ, solid) and water vapor mixing ratio (r, dashed) illustrating three atypical case types: (a–c) not-well-mixed, (d–f) ambiguous h_2, and (g–i) $\theta - r$ decoupled. Horizontal lines denote key convective boundary layer (CBL) parameters: The entrainment zone (EZ) bottom (h_0, red), EZ top (h_2, blue), boundary-layer height (zi, purple), and surface-layer top (z_{SL}, green). Profiles are drawn from both the IHOP_2002 and ARM SGP (2009) datasets.). AGL, above ground level [Colour figure can be viewed at wileyonlinelibrary.com]

comparable to those inferred from previous LES and observational studies, where inversion jumps of 4–8 K and 2–3 $\mathrm{g \cdot kg^{-1}}$ across 100–300-m thick layers yield similar order-of-magnitude estimates (Huang *et al.*, 2011; Sullivan *et al.*, 1998).

The algorithm is applicable across daytime convective conditions, from the late morning growth phase to the mature CBL period. During the late morning hours, when the CBL is still developing, the algorithm can retrieve physically consistent CBL parameters in many cases; however,

TABLE 2 Summary statistics of convective boundary layer (CBL) parameters derived from canonical soundings in the high-resolution datasets (110 soundings: 38 from IHOP_2002 ISS and 72 from ARM SGP CF) and the Korea Meteorological Administration (KMA) dataset (48 soundings)

	High-resolution		KMA	
Parameter	Mean	Median	Mean	Median
z_{SL} [m]	89	83	108	83
z_i [m]	1168	1066	1325	1300
ΔEZ [m]	257	210	291	237
$^{\Delta\theta}/_{\Delta EZ}$ [K·m^{-1}]	0.019	0.013	0.012	0.01
$\lvert ^{\Delta r}/_{\Delta EZ}\rvert$ [g·kg^{-1}·m^{-1}]	0.024	0.015	0.014	0.011

Note: Among these, z_{SL} is available for 85 and 41 cases in the high-resolution and KMA datasets, respectively, after excluding soundings without a well-defined surface layer.

profiles during this period frequently exhibit structural characteristics of a developing CBL rather than those of a fully canonical CBL, leading to a higher fraction of atypical classification. Even in these cases, the retrieved parameters remain physically interpretable estimates of key CBL features. Preliminary inspection of soundings outside the analyzed period suggests that during the early morning and evening transition periods, deviations from the typical CBL structure become more pronounced, limiting the reliability of parameter estimation with the algorithm.

3.2 | Operational radio soundings

We also applied the wavelet approach to radio soundings from the Osan WMO upper-air station operated by the Korea Meteorological Administration (KMA) in South Korea (37.09° N, 127.03° E). The Osan station conducts routine launches four times daily at 0000, 0600, 1200, and 1800 UTC. For this study, we analyzed the 0600 UTC (1500 LST) soundings from May to September 2019, yielding a total of 150 profiles.

These operational soundings provide routine vertical profiles of temperature and humidity, but their vertical resolution is substantially coarser than that of the IHOP_2002 ISS and ARM SGP CF datasets. The relatively sparse sampling tends to smooth the vertical gradients of θ and r, thereby weakening the covariance signal used by the algorithm and potentially leading to misidentification of CBL parameters. Nevertheless, such soundings remain valuable for examining broader variability and extracting key CBL characteristics under operational monitoring conditions. Consistent with this limitation, Seidel *et al.* (2010) showed that sparse vertical sampling introduces structural uncertainties in boundary layer height estimation, while Guo *et al.* (2021), using a bulk Richardson number method, demonstrated that insufficient vertical resolution smooths the thermodynamic gradients near the CBL top and degrades the accuracy of height detection.

Despite these limitations, 48 of the 150 KMA soundings (32%) exhibited canonical CBL structures, for which the algorithm produced reliable estimates (Figure 11a–d). This result demonstrates the method can capture key CBL characteristics even from coarse-resolution operational data. The statistical properties of the estimated CBL parameters for these canonical cases are summarized in Table 2 and are comparable in magnitude to those derived from the high-resolution dataset.

For the remaining atypical profiles discussed in the previous section, the algorithm still yielded reasonable estimates, as illustrated in Figure 11e–h. These examples suggest that even when coarse vertical resolution smooths thermodynamic gradients, the method can still provide meaningful results when distinct thermodynamic transitions remain identifiable at the SL–ML, and ML–EZ interfaces. However, as shown in Figure 11h, the method may overestimate the EZ base height (h_0) when a strong negative covariance signal develops in the upper free atmosphere, highlighting an inherent limitation of the approach.

Figure 12 presents vertical profiles of θ and r normalized by their ML mean values (θ_{ML} and r_{ML}) and plotted against height normalized by the CBL height (z/z_i). Here, θ_{ML} and r_{ML} were calculated over the layer between z_{SL} and h_0. For the high-resolution datasets, 85 of the 110 canonical soundings with well-defined SL structures were used, whereas for the KMA dataset, 41 of the 48 soundings exhibiting clear SL structures were included. These normalized profiles demonstrate how multiple CBL soundings can be summarized using the scaling parameters, θ_{ML}, r_{ML}, and z_i, enabling a normalized representation of the mean CBL structure. The composite profiles derived from the high-resolution and KMA datasets reveal systematic differences reflecting variations in CBL characteristics and boundary conditions, including surface thermal and moisture properties and the lapse rate of the overlying free atmosphere. The corresponding statistics of these scaling parameters are summarized in Table 3.

3.3 | Sensitivity of the algorithm to vertical resolution

To assess the sensitivity of the algorithm to vertical resolution, we conducted an under-sampling experiment using

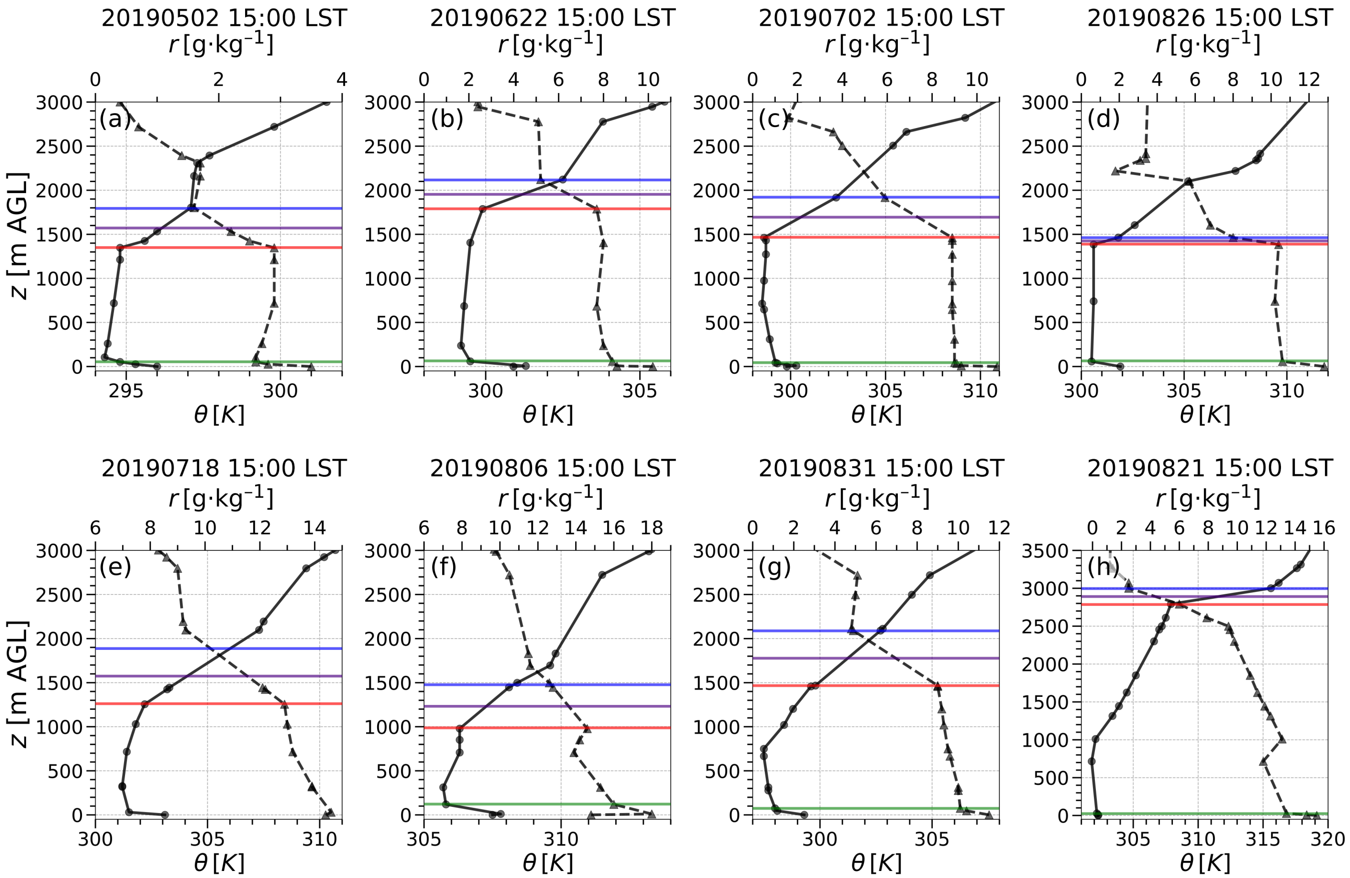

FIGURE 11 Vertical profiles of potential temperature (θ, solid) and water vapor mixing ratio (r, dashed) selected from Korea Meteorological Administration (KMA) soundings. Canonical convective boundary layer (CBL) conditions are shown in panels (a–d), whereas panels (e–h) illustrate atypical conditions: (e) weak entrainment, (f) not-well-mixed, (g) $\theta - r$ decoupled, and (h) h_0 overestimation. The markers indicate the observed values with circles for θ and triangles for r. Horizontal lines denote key CBL parameters: the entrainment-zone (EZ) bottom (h_0, red), EZ top (h_2, blue), boundary-layer height (zi, purple), and surface-layer (SL) top (z_{SL}, green). AGL, above ground level [Colour figure can be viewed at wileyonlinelibrary.com]

FIGURE 12 Vertical profiles of normalized (a) potential temperature (θ/θ_{ML}) and (b) water vapor mixing ratio (r/r_{ML}) as a function of normalized height (z/z_i), derived from canonical soundings. Profiles from the high-resolution datasets (85 soundings) are shown in blue, and those from the Korea Meteorological Administration (KMA) dataset (41 soundings) are shown in red. Solid lines denote the mean profiles, while shaded regions represent one standard deviation about the mean. [Colour figure can be viewed at wileyonlinelibrary.com]

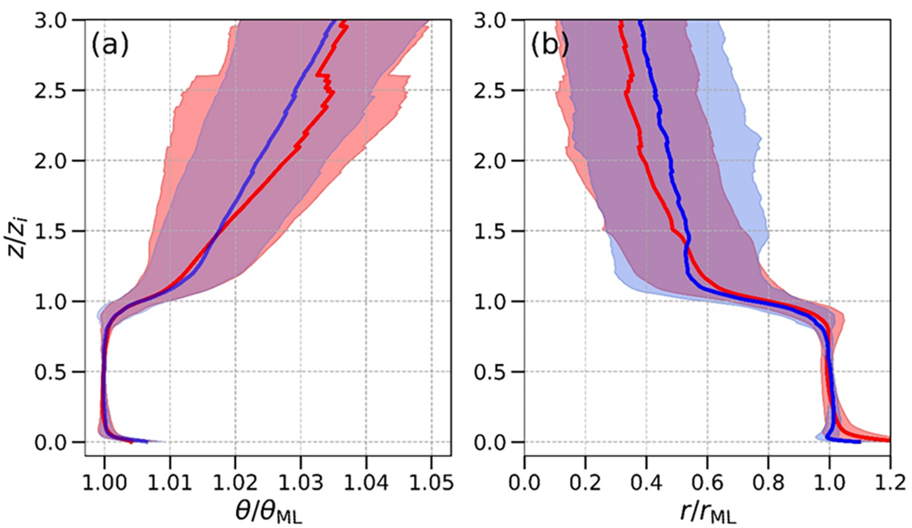

high-resolution profiles modified to emulate the vertical level discretization of operational radiosonde observations. While we recognize that this experiment is based on a limited number of selected cases and may not fully capture the entire spectrum of operational sounding resolutions, the primary objective was to examine how insufficient sampling within the SL and EZ affects the detection of key CBL parameters. To this end, two high-resolution

TABLE 3 Statistical summary (mean, median, and standard deviation) of mixed-layer (ML) scaling parameters derived from the high-resolution datasets (85 soundings) and the Korea Meteorological Administration (KMA) dataset (41 soundings)

	High-resolution soundings			KMA soundings		
Statistic	θ_{ML} [K]	r_{ML} [g · kg^{-1}]	z_i [m]	θ_{ML} [K]	r_{ML} [g · kg^{-1}]	z_i [m]
Mean	305	10.5	1184	298	8.4	1313
Median	305	10.7	1068	298	7.9	1288
Standard deviation	6.14	2.7	484.4	3.7	3.2	481.2

TABLE 4 Vertical resolution of two operational radiosonde profiles used in the under-sampling experiment

Region	Statistics		Fine-resolution case	Coarse-resolution case
EZ (1–3 km)	Number of levels		16	4
	Vertical spacing	Mean [m]	130	551
		Min. [m]	10	30
		Max. [m]	307	1042
SL (0–500 m)	Number of levels		5	2
	Vertical spacing	Mean [m]	28	279
		Min. [m]	16	279
		Max. [m]	44	279

Note: For each case, the number of height levels, and the mean, minimum, and maximum vertical spacing (Δz, m) are listed. The fine-resolution case is based on the profile observed at 15:00 LST on 28 August 2019, and the coarse-resolution case on the profile observed at 15:00 LST on 20 July 2019. These two soundings represent the densely and sparsely sampled conditions within the Korea Meteorological Administration (KMA) dataset. EZ, entrainment zone; SL, surface layer

reference profiles were selected: one from the IHOP_2002 Homestead site (12:15 LST, 13 May 2002) and another from the ARM SGP CF (11:30 LST, 21 May 2009). Both were previously identified as canonical CBL cases (Figure 9a,d) that resolve the essential SL, ML, and EZ structures.

To reproduce the vertical reporting characteristics of operational radiosonde, the high-resolution profiles were resampled using the vertical level structures from two selected KMA soundings, which include both mandatory and significant levels. While mandatory levels correspond to standard pressure levels, significant levels represent additional points reported where strong gradients in temperature and humidity occur. Recognizing that these two soundings do not encompass all possible operational reporting scenarios, they were specifically selected to represent contrasting sampling configurations: a relatively dense case (15:00 LST, 28 August 2019) and a sparse case (15:00 LST, 20 July 2019). This selection was based on the vertical spacing and the density of reported levels within and around the SL and EZ, providing a focused basis for sensitivity analysis. The corresponding vertical-level distributions are summarized in Table 4.

Figure 13 illustrates the algorithm's sensitivity to vertical resolution using these canonical profiles. The original high-resolution profiles (Figure 13a,d) were resampled according to the vertical levels of selected KMA soundings to evaluate potential diagnostic discrepancies. While we acknowledge that the results in Figure 13 are derived from a limited set of cases and may not represent the full variability of all potential sounding environments, the comparison clearly demonstrates how variations in sampling density, particularly within and around the SL and EZ, can alter the representation of the original profiles and significantly affect the diagnosed CBL parameters. This focused illustration serves to highlight the inherent sensitivity of the algorithm to the vertical resolution provided by operational reporting systems.

In the relatively fine-resolution case (mean vertical spacing of approximately 130 m in the EZ and 28 m in the SL; Table 4, Figure 13b,e), the down-sampled profiles still capture the key gradients of the original soundings. For the 13 May 2002 case, the diagnosed SL height (z_{SL}) is identical to that obtained from the original profile. Although the EZ depth (ΔEZ) differs by about 100 m, the CBL top (z_i) differs by only about 15 m and the overall EZ structure remains consistent.

In contrast, the coarse-resolution case (mean vertical spacing of approximately 551 m in the EZ and 279 m in the SL; Table 4, Figure 13c,f) substantially degrades the representation of the vertical structure. Sparse sampling leaves

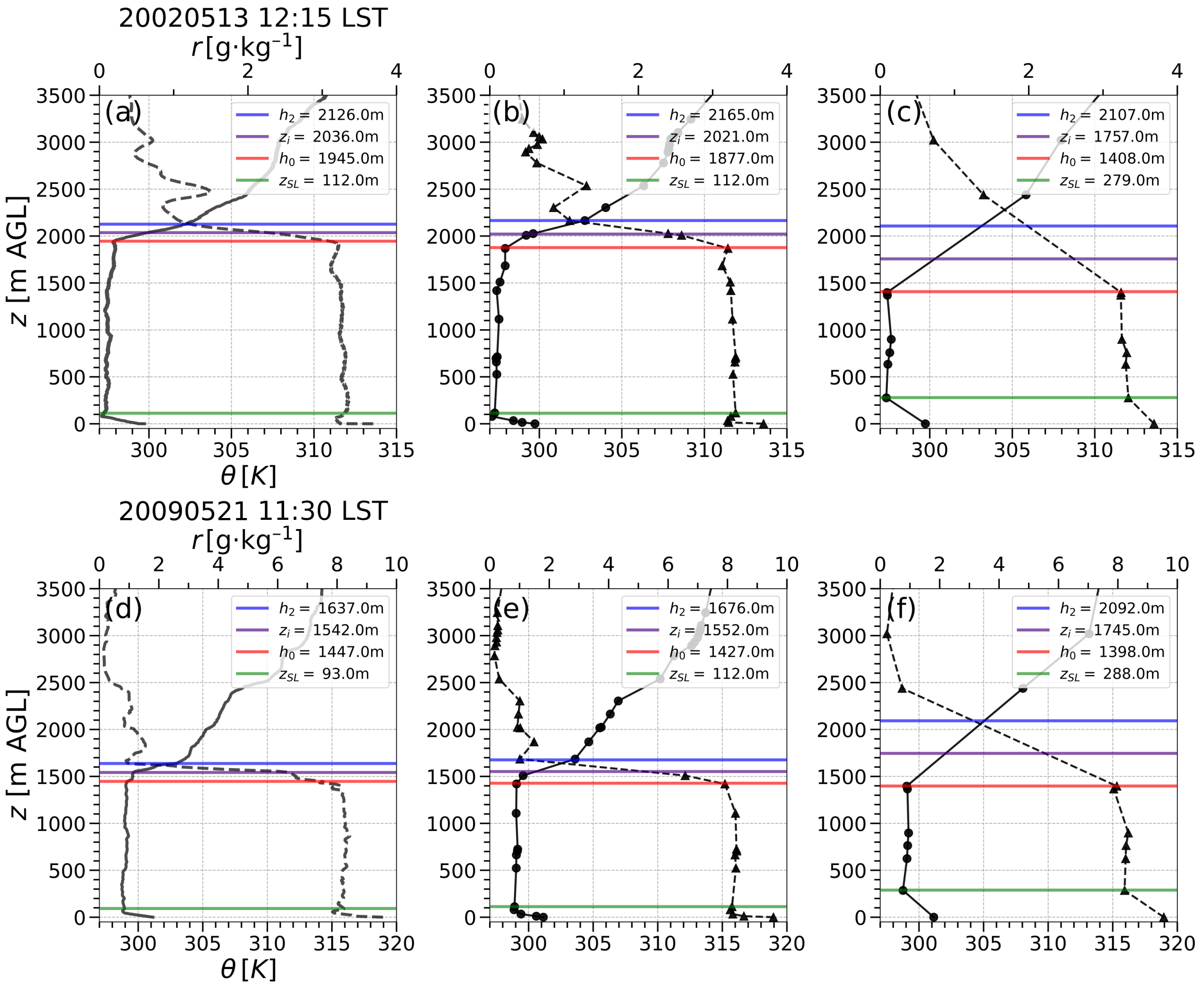

FIGURE 13 Algorithm performance under different vertical resolutions for the two canonical profiles shown in Figure 9. The first column (a, d) presents the original high-resolution profiles; the second column (b, e) shows the profiles down-sampled using the vertical level structure of the KMA radiosonde sounding observed at 15:00 LST on 28 August 2019 (relatively finer vertical sampling); and the third column (c, f) shows profiles down-sampled using the vertical level structure of the KMA sounding observed at 15:00 LST on 20 July 2019 (relatively coarser vertical sampling). Horizontal lines denote key CBL parameters: Entrainment zone (EZ) bottom (h_0, red), EZ top (h_2, blue), boundary-layer height (zi, purple), and the surface-layer top (z_{SL}, green). AGL, above ground level [Colour figure can be viewed at wileyonlinelibrary.com]

only two reported levels below 300 m, which is insufficient to resolve the vertical gradients of θ and r required to detect z_{SL}. Consequently, the algorithm diagnoses z_{SL} at much higher levels and misrepresents the EZ structure.

To quantify this sensitivity more systematically, a vertical-thinning experiment was performed using multiple high-resolution sounding observations. The original profiles, interpolated to a uniform 5 m spacing, were resampled at vertical intervals ranging from 5 m (default) to 500 m in 25-m increments (i.e., 25–500 m), with an additional case at 15 m. The algorithm was applied to each resampled profile, and the resulting CBL parameters were compared with those obtained from the original profiles. This analysis used 38 typical soundings from the IHOP_2002 dataset and 72 soundings from the ARM SGP dataset (Table 1).

Figure 14a shows the mean absolute error (MAE) of the estimated z_i, relative to the default 5-m resolution. The median and the interquartile range (25th–75th percentiles) of the absolute errors are also presented for each vertical grid spacing. For all spacings, the median values are smaller than the mean, indicating a positively skewed

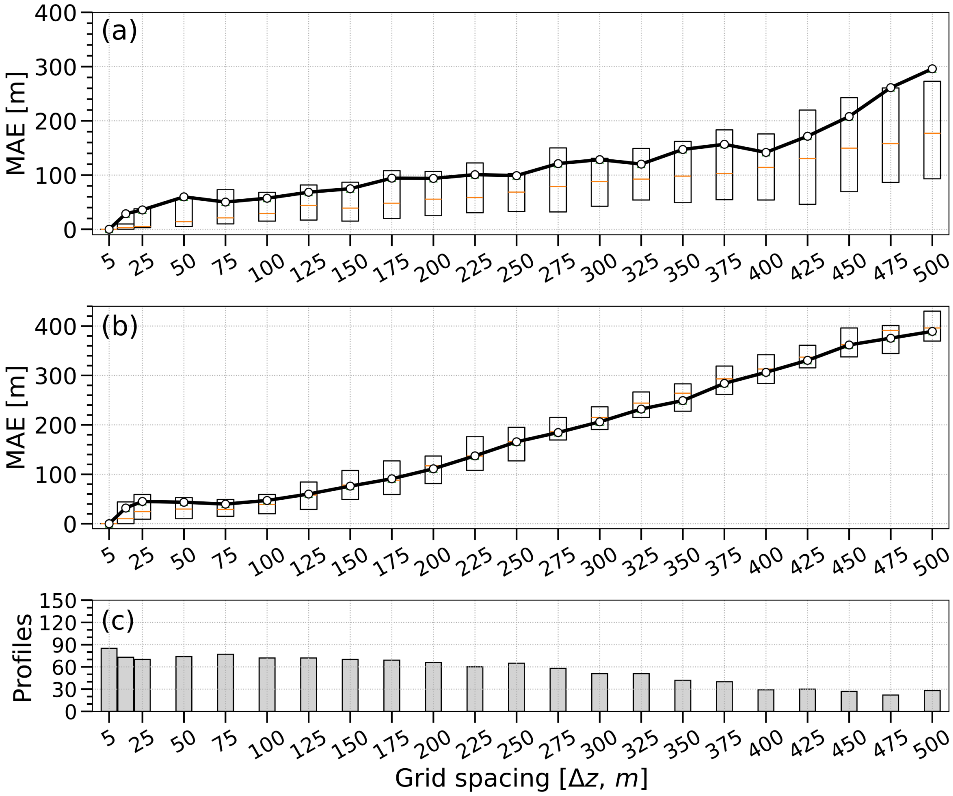

FIGURE 14 Distribution of the absolute error in (a) boundary-layer height (z_i) and (b) surface-layer height (z_{SL}) as a function of vertical grid spacing (Δz). Boxplots indicate the error distribution, and the horizontal line and open circles represent the median and mean absolute error (MAE), respectively. Panel (c) shows the number of profiles used in the calculation for z_{SL} at each grid spacing. The analysis is based on 110 canonical soundings, while the number of available profiles for z_{SL} ranges from 85 to 22 depending on Δz. [Colour figure can be viewed at wileyonlinelibrary.com]

error distribution with a relatively small number of large errors. The MAE remains below 75 m for spacings up to 150 m, rises to about 100 m at 200 m spacing, gradually increases to approximately 150 m for spacings between 300 and 400 m, and exceeds 200 m at 475 m. Overall the covariance-based estimation of z_i shows relatively weak sensitivity to vertical resolution, with the MAE remaining below approximately 200 m even at a spacing of 400 m. Given the mean and median z_i values of 1168 m and 1066 m (Table 2), these errors correspond to about $0.09z_i$ for an MAE of 100 m and about 0.17–$0.19z_i$ for an MAE of 200 m.

These results suggest that reliable detection of CBL structure requires vertical sampling intervals smaller than the typical EZ depth (about 200 m). In practice, vertical spacings on the order of 100 m to about 200 m are generally sufficient to reproduce key CBL parameters with reasonable accuracy, whereas spacings of several hundred meters lead to progressively larger uncertainties. In contrast to z_i, the MAE of z_{SL} (Figure 14b) increases much more rapidly with increasing vertical grid spacing. The MAE remains below 50 m for spacings up to 100 m but rises sharply thereafter, reaching 166 m at 250 m. As vertical spacing becomes coarser, the smoothing of vertical gradients also reduces the number of soundings in which z_{SL} can be detected (Figure 14c). Nevertheless, more than 60 of 85 soundings (approximately 70%) remain available at spacings up to 250 m, indicating that the reduction in sample size does not yet undermine the statistical robustness of the analysis. Given the mean and median z_{SL} values of 89 and 83 m (Table 2), this error is roughly twice the typical z_{SL} depth. These results indicate that reliable estimation of z_{SL} requires vertical spacings finer than about 100 m.

Taken together, the case study analysis (Figure 13) and the statistical evaluation based on multiple soundings (Figure 14) consistently demonstrate that the reliability of the covariance-based algorithm depends strongly on vertical sampling density. When the vertical resolution is sufficiently fine, the algorithm reproduces key CBL parameters in close agreement with the original high-resolution profiles. In contrast, sparse vertical sampling weakens the representation of thermodynamic gradients within the SL and EZ, leading to increased uncertainty in the diagnosed parameters. The statistical results further show that the estimation of z_i remains relatively robust to vertical resolution, whereas the estimation of z_{SL} is considerably more sensitive to coarse vertical sampling.

3.4 | Comparisons with the gradient method

To clarify the structural advantages of the proposed covariance-based framework, we compare it with the conventional maximum-gradient method for diagnosing the CBL top z_i, defined as the altitude where the vertical

TABLE 5 Summary statistics of the absolute differences in convective boundary layer (CBL) height ($|\Delta z_i|$) between the covariance-based method and maximum-gradient methods using potential temperature (θ), virtual potential temperature (θ_v), and water vapor mixing ratio (r).

Category	Gradient variable	$\|\Delta z_i\|$ [m] Mean	Median	Min.	Max.
1	θ	106	46	0	1604
	θ_v	210	54	0	2102
	r	213	49	1	2214
2	θ	445	159	88	1325
	θ_v	356	159	88	1330
	r	1005	838	107	2459
3	θ	1141	1041	20	3069
	θ_v	1065	611	85	3069
	r	514	121	20	2392

Note: The analysis is based on the 110 canonical soundings, of which 87 were classified into three categories according to the relative strength of temperature and moisture gradients near the entrainment zone: $\theta - r$ coupled (61 cases), θ-dominant (6 cases), and r-dominant (20 cases).

gradient of a selected scalar variable attains its maximum magnitude. To examine the sensitivity of diagnosed CBL height to the choice of variable, the maximum-gradient method was applied to vertical profiles of θ, θ_v, and r from the 110 canonical cases selected from the IHOP_2002 and ARM SGP soundings. Three representative EZ structures were identified manually by visual inspection of the profiles and classified according to the relative strength and vertical alignment of the θ and r gradients: (1) Category 1, distinct and vertically collocated gradients in both θ and r; (2) Category 2, strong θ gradient with weak r gradient; and (3) Category 3, strong r gradient with weak θ gradient.

For a controlled comparison, only high-resolution profiles that clearly exhibit one of these structures were selected, yielding 87 cases in total: 61 in Category 1 (e.g., 13 May 2002; Figure 9a, and 21 May 2009; Figure 9d), 6 in Category 2 (e.g., 17 June 2009; Figure 9c, and 3 September 2009; Figure 9e), and 20 in Category 3 (e.g., 16 June 2002; Figure 9b, and 2 August 2009; Figure 9f). Among the 110 canonical cases, 23 profiles with ambiguous or mixed gradient characteristics were excluded. The CBL heights diagnosed from each variable were compared across these categories, and their distributions were summarized using standard statistics (mean, median, minimum, and maximum) as reported in Table 5.

In most previous studies, the maximum-gradient method has been applied to θ or virtual potential temperature (θ_v) (e.g., Holzworth, 1964; Li, Liu, *et al.*, 2021; Li, Zhang, *et al.*, 2021; Seidel *et al.*, 2010). Under typical CBL conditions, however, differs only slightly from θ, because the virtual correction depends on r, which is small compared to unity (Stull, 1988). As a result, profiles closely resemble θ profiles. Consistent with this, the gradient-based estimates of z_i derived from θ and are similar (Table 5). In Category 1, the median differences between the gradient-based and the covariance-based estimates of z_i are small (46 and 56 m for θ and θ_v, respectively). In Category 2, the corresponding median differences are identical (159 m). In Category 3, where the θ gradient becomes ambiguous, both estimates deviate substantially from the covariance-based z_i, with mean differences of 1141 and 1065 m and median differences of 1041 and 611 m for the θ and θ_v-based estimates, respectively.

In contrast, the use of r alone for maximum-gradient-based detection of the CBL height has been relatively rare. Most operational and research applications primarily rely on thermal variables, operating under the implicit assumption that temperature gradients adequately represent the CBL top (Guo *et al.*, 2021; Seidel *et al.*, 2010). Observations, however, often show that moisture transitions across the entrainment zone can be sharper than, or vertically displaced from, temperature transitions, particularly under conditions of dry-air entrainment or residual-layer influence (Bennett *et al.*, 2010; Sullivan *et al.*, 1998).

Table 5 shows that the gradient-based and covariance-based estimate fall within a narrow vertical range when the maximum temperature and moisture gradients are vertically collocated (Category 1), with a median difference of approximately 50 m. Under these conditions, all three gradient-based estimates converge. In contrast, when the temperature and moisture gradients are vertically displaced (Categories 2 and 3), clear differences emerge among the estimates. In Category 2, the θ-based estimates remain more consistent with the covariance-based estimates, showing a median difference of about 160 m (Table 5). In contrast, the r-based estimates diverge substantially, with a median difference of roughly 800 m (Table 5). In Category 3, the opposite pattern emerges: the θ-based estimates show a median difference of about 1000 m, whereas the r-based estimates exhibit a much smaller median difference of roughly 100 m (Table 5). These results demonstrate that the maximum-gradient method is inherently sensitive to the choice of a variable and may diagnose different potions of the EZ depending on the variable used.

This sensitivity arises because the maximum-gradient method identifies the altitude of the strongest gradient of a single scalar field. For example, in the 23 May 2002 case (Figure 10g), the maximum gradient of r occurs at 1444 m, whereas the strongest gradient of θ occurs near 2578 m. The latter altitude does not appear to correspond to the CBL top but simply marks the largest θ gradient.

These heights therefore represent different gradient maxima rather than a uniquely defined CBL top. This example illustrates how the gradient method can identify different parts of the profile depending on the variable considered.

The covariance-based method overcomes this limitation by simultaneously incorporating both θ and r within the Haar DWT framework. Rather than identifying a single gradient extremum, it detects the scale-localized extremum of the θ–r covariance that characterizes the EZ as a layer of anticorrelated thermodynamic and moisture structure (Stull, 1988; Sullivan & Patton, 2011). The method identifies both the lower and upper bounds of the EZ based on this coupled transition and defines the CBL height as the midpoint between these two dynamically meaningful boundaries. Consequently, the diagnosed z_i reflects the finite-depth structure of the EZ rather than a single extremum within it.

4 | CONCLUSIONS

This study developed and applied a wavelet-based framework for extracting key CBL parameters from radio soundings. By using the Haar discrete wavelet transform (DWT), vertical profiles of potential temperature and r were decomposed into multiscale segment means and deviations. This approach provides a systematic way to diagnose the SL top, EZ boundaries, and CBL height from scale-dependent covariance signals, thereby extending traditional gradient- and parcel-based methods with an objective, multiresolution tool. Applications to high-resolution radio soundings from IHOP_2002 and the ARM SGP Central Facility demonstrated that the algorithm can reliably capture canonical CBL structures. In these cases, the diagnosed heights of the SL, EZ, and CBL top closely matched visual inspection, confirming the physical robustness of the method. The wavelet approach also distinguished atypical and ambiguous profiles, where strong mixed-layer fluctuations, diffuse gradients, or θ–r decoupling reduced diagnostic clarity. Such cases illustrate both the capability of the method to flag departures from canonical structure and its limitations when applied to complex boundary-layer conditions. The analysis further revealed that vertical resolution is a critical factor. Fine-resolution profiles preserved the sharp gradients required for reliable detection, yielding parameter estimates closely aligned with those from high-resolution reference data. In contrast, coarse-resolution profiles tended to smooth these gradients, introducing biases in the diagnosed SL height and EZ depth. Even so, the algorithm provided the most consistent estimates attainable under such conditions, demonstrating its practical utility for extending boundary-layer characterization to routine operational datasets. Overall, the Haar wavelet framework offers a versatile and objective methodology for quantifying CBL structure across a wide range of observational settings. Its consistent performance on both research-grade and operational soundings underscores its value for process studies, long-term climatological assessments, and model evaluation. Future developments will focus on improving the treatment of atypical cases, incorporating additional radiosonde variables such as wind speed and direction, and extending applications across broader observational networks to establish robust climatological baselines of boundary-layer variability.

ACKNOWLEDGEMENTS

This study was supported by the Basic Science Research Program through the National Research Foundation of Korea (NRF), funded by the Ministry of Education (RS-2021-NR060132); the Korean Meteorological Administration Research and Development Program (RS-2024-00404042); and the Regional Innovation System and Education (RISE) Program through the Gangwon RISE Center, funded by the Ministry of Education and the Gangwon State, Republic of Korea (2026-RISE-10-002).

FUNDING INFORMATION

This study was supported by the Basic Science Research Program through the National Research Foundation of Korea (NRF), funded by the Ministry of Education (RS-2021-NR060132); the Korean Meteorological Administration Research and Development Program (RS-2024-00404042); and the Regional Innovation System and Education (RISE) Program through the Gangwon RISE Center, funded by the Ministry of Education and the Gangwon State, Republic of Korea (2026-RISE-10-002).

DATA AVAILABILITY STATEMENT

The data that support the findings of this study are openly available from the following sources. The IHOP_2002 radiosonde observations are available from the Earth Observing Laboratory (EOL) Field Data Archive at https://doi.org/10.5065/D66T0K1J. Radiosonde observations from the ARM Southern Great Plains (SGP) site are available from the ARM user facility data archive (https://doi.org/10.5439/1595321). The Korea Meteorological Administration (KMA) radiosonde observations are accessible through the KMA Data Portal API Hub (https://apihub.kma.go.kr/) under the upper-air observation dataset.

ORCID

Song-Lak Kang https://orcid.org/0000-0002-3947-2211
Cho-Rong Choi https://orcid.org/0009-0007-2707-0817
Jung-Hee Ryu https://orcid.org/0000-0003-2441-151X

REFERENCES

Baars, H., Ansmann, A., Engelmann, R. & Althausen, D. (2008) Continuous monitoring of the boundary-layer top with lidar. *Atmospheric Chemistry and Physics*, 8, 7281–7296. Available from: https://doi.org/10.5194/acp-8-7281-2008

Bennett, L.J., Weckwerth, T.M., Blyth, A.M., Banta, R.M., Shapiro, M.D., LeMone, M.A. et al. (2010) Observations of the evolution of the nocturnal and convective boundary layers and the structure of open-celled convection on 14 June 2002. *Monthly Weather Review*, 138, 2589–2607. Available from: https://doi.org/10.1175/2010MWR3200.1

Berg, L.K. & Lamb, P.J. (2016) Surface properties and interactions: coupling the land and atmosphere within the ARM program. *Meteorological Monographs*, 57, 21–23. Available from: https://doi.org/10.1175/AMSMONOGRAPHS-D-15-0044.1

Brooks, I.M. (2003) Finding boundary layer top: application of a wavelet covariance transform to lidar backscatter. *Journal of Atmospheric and Oceanic Technology*, 20, 1092–1105. Available from: https://doi.org/10.1175/1520-0426(2003)020<1092:FBLTAO>2.0.CO;2

Cohn, S.A. & Angevine, W.M. (2000) Boundary layer height and entrainment zone thickness measured by lidars and wind-profiling radars. *Journal of Applied Meteorology*, 39, 1233–1247. Available from: https://doi.org/10.1175/1520-0450(2000)039<1233:BLHAEZ>2.0.CO;2

Conzemius, R.J. & Fedorovich, E. (2008) A case study of convective boundary layer development during IHOP_2002: numerical simulations compared to observations. *Monthly Weather Review*, 136, 2305–2320. Available from: https://doi.org/10.1175/2007MWR2193.1

Couvreux, F., Guichard, F., Redelsperger, J.-L., Kiemle, C., Masson, V., Lafore, J.-P. et al. (2005) Water-vapour variability within a convective boundary layer assessed by large-eddy simulations and IHOP_2002 observations. *Quarterly Journal of the Royal Meteorological Society*, 131, 2665–2693. Available from: https://doi.org/10.1256/qj.04.167

Davis, K.J., Gamage, N., Hagelberg, C.R., Kiemle, C., Lenschow, D.H. & Sullivan, P.P. (2000) An objective method for deriving atmospheric structure from airborne lidar observations. *Journal of Atmospheric and Oceanic Technology*, 17, 1455–1468. Available from: https://doi.org/10.1175/1520-0426(2000)017<1455:AOMFDA>2.0.CO;2

García-Franco, J.L., Osprey, S. & Gray, L.J. (2021) A wavelet transform method to determine monsoon onset and retreat from precipitation time-series. *International Journal of Climatology*, 41(11), 5295–5317. Available from: https://doi.org/10.1002/joc.7130

Guo, J., Zhang, J., Yang, K., Liao, H., Zhang, S., Huang, K. et al. (2021) Investigation of near-global daytime boundary layer height using high-resolution radiosondes: first results and comparison with ERA5, MERRA-2, JRA-55, and NCEP-2 reanalyses. *Atmospheric Chemistry and Physics*, 21, 17079–17097. Available from: https://doi.org/10.5194/acp-21-17079-2021

Holzworth, G.C. (1964) Estimates of mean maximum mixing depths in the contiguous United States. *Monthly Weather Review*, 92(5), 235–242. Available from: https://doi.org/10.1175/1520-0493(1964)092<0235:EOMMMD>2.3.CO;2

Huang, J., Lee, X. & Patton, E.G. (2011) Entrainment and budgets of heat, water vapor, and carbon dioxide in a convective boundary layer driven by time-varying forcing. *Journal of Geophysical Research*, 116, D06308. Available from: https://doi.org/10.1029/2010JD014938

Kaimal, J.G. & Finnigan, J.J. (1994) *Atmospheric boundary layer flows: their structure and measurements*. New York: Oxford University Press.

Kakkanattu, S.P., Mehta, S.K., Purushotham, P., Betsy, K.B., Seet ha, C.J. & Musaid, P.P. (2023b) Continuous monitoring of the atmospheric boundary layer (ABL) height from micro pulse lidar over a tropical coastal station, Kattankulathur (12.82° N, 80.04° E). *Meteorology and Atmospheric Physics*, 135(2), 2. Available from: https://doi.org/10.1007/s00703-022-00938-x

Kakkanattu, S.P., Mehta, S.K., Balasubrahamanyam, D., Rakesh, V. & Kesarkar, A.P. (2023a) Thermodynamic structure of the atmospheric boundary layer over a Coastal Station in India for contrasting sky conditions during different seasons. *Atmospheric Research*, 293, 293106915. Available from: https://doi.org/10.1016/j.atmosres.2023.106915

Lee, J. & Pal, S. (2021) Impacts of measurement errors on planetary boundary layer height estimation from radiosonde profiles. *Journal of Atmospheric and Oceanic Technology*, 38, 197–210. Available from: https://doi.org/10.1175/JTECH-D-20-0086.1

LeMone, M.A., Chen, F., Alfieri, J.G., Cuenca, R.H., Hagimoto, Y., Blanken, P. et al. (2007) NCAR/CU surface, soil, and vegetation observations during the international H2O project 2002 field campaign. *Bulletin of the American Meteorological Society*, 88, 65–82. Available from: https://doi.org/10.1175/BAMS-88-1-65

Li, H., Liu, B., Ma, X., Jin, S., Ma, Y., Zhao, Y. et al. (2021) Evaluation of retrieval methods for planetary boundary layer height based on radiosonde data. *Atmospheric Measurement Techniques*, 14(9), 5977–5986. Available from: https://doi.org/10.5194/amt-14-5977-2021

Li, H., Zhang, B., Huang, X. & Ding, Z. (2021) Evaluation of four commonly used methods for estimating planetary boundary layer height from radiosonde measurements. *Atmospheric Measurement Techniques*, 14, 6853–6867. Available from: https://doi.org/10.5194/amt-14-6853-2021

Mehta, S.K., Ratnam, M.V., Sunilkumar, S.V., Narayana Rao, D. & Krishna Murthy, B.V. (2017) Diurnal variability of the atmospheric boundary layer height over a tropical station in the Indian monsoon region. *Atmospheric Chemistry and Physics*, 17, 531–549. Available from: https://doi.org/10.5194/acp-17-531-2017

Richardson, L.F. (1920) The supply of energy from and to atmospheric eddies. *Proceedings of the Royal Society of London. Series A, Containing Papers of a Mathematical and Physical Character*, 97(686), 354–373.

Richardson, S.J., Basu, S. & Holtslag, A.A.M. (2013) Improving stable boundary-layer height estimation using a stability-dependent critical bulk Richardson number. *Boundary-Layer Meteorology*, 148, 93–109. Available from: https://doi.org/10.1007/s10546-013-9812-3

Schmid, P. & Niyogi, D. (2012) A method for estimating planetary boundary layer heights and its application over the ARM southern Great Plains site. *Journal of Atmospheric and Oceanic Technology*, 29, 316–322. Available from: https://doi.org/10.1175/JTECH-D-11-00118.1

Seidel, D.J., Ao, C.O. & Li, K. (2010) Estimating climatological planetary boundary layer heights from radiosonde observations:

comparison of methods and uncertainty analysis. *Journal of Geophysical Research*, 115, D16113. Available from: https://doi.org/10.1029/2009JD013680

Stouffer, B.C., Stensrud, D.J. & Zhang, Y. (2025) Estimates of entrainment zone depth across the United States from dual-polarization WSR-88D radar observations. *Monthly Weather Review*, 153(12), 2829–2843. Available from: https://doi.org/10.1175/MWR-D-25-0146.1

Stull, R.B. (1988) *An introduction to boundary layer meteorology*. Dordrecht, Boston, MA and London: Springer.

Sullivan, P.P., Moeng, C.-H., Stevens, B., Lenschow, D.H. & Mayor, S.D. (1998) Structure of the entrainment zone capping the convective atmospheric boundary layer. *Journal of the Atmospheric Sciences*, 55, 3042–3064. Available from: https://doi.org/10.1175/1520-0469(1998)055<3042:SOTEZC>2.0.CO;2

Sullivan, P.P. & Patton, E.G. (2011) The effect of mesh resolution on convective boundary layer statistics and structures generated by large-eddy simulation. *Journal of the Atmospheric Sciences*, 68(10), 2395–2415. Available from: https://doi.org/10.1175/JAS-D-10-05010.1

Vickers, D. & Mahrt, L. (2003) The cospectral gap and turbulent flux calculations. *Journal of Atmospheric and Oceanic Technology*, 20(5), 660–672. Available from: https://doi.org/10.1175/1520-0426(2003)20<660:TCGATF>2.0.CO;2

Vogelezang, D.H.P. & Holtslag, A.A.M. (1996) Evaluation and model impacts of alternative boundary-layer height formulations. *Boundary-Layer Meteorology*, 81(3), 245–269. Available from: https://doi.org/10.1007/BF02430331

Wang, X.Y. & Wang, K.C. (2014) Estimation of atmospheric mixing layer height from radiosonde data. *Atmospheric Measurement Techniques*, 7, 1701–1712. Available from: https://doi.org/10.5194/amt-7-1701-2014

Wang, Y., Zhao, T., Zhou, D. & Wang, W. (2014) An improved method for estimating mixing layer height from radiosonde profiles. *Atmospheric Measurement Techniques*, 7, 1701–1709. Available from: https://doi.org/10.5194/amt-7-1701-2014

Weckwerth, T.M., Parsons, D.B., Koch, S.E., Moore, J.A., LeMone, M.A., Demoz, B.B. et al. (2004) An overview of the international H2O project (IHOP_2002) and some preliminary highlights. *Bulletin of the American Meteorological Society*, 85, 253–277. Available from: https://doi.org/10.1175/BAMS-85-2-253

How to cite this article: Kang, S.-L., Choi, C.-R. & Ryu, J.-H. (2026) Wavelet covariance approach to measure convective boundary-layer structure. *Quarterly Journal of the Royal Meteorological Society*, e70248. Available from: https://doi.org/10.1002/qj.70248